ABSTRACT

Title of Thesis: THE INFLUENCE OF WIND ON THE STRUCTURE OF INCLINED FLAMES

Michael V. Heck
Master of Science, 2020

Thesis directed by: Professor Michael Gollner
Department of Fire Protection Engineering

Experiments were performed using stationary gas burners in order to characterize the flame geometry and downstream heating from stationary flames under inclined configurations under an applied forced flow. Stationary flames exhibit behavior similar to spreading wildland fires but are an ideal configuration for carefully studying fundamental wildland fire behaviour characteristics that play a critical role in downstream heating, which subsequently drive fire spread. Two conditions were applied to a small-scale apparatus during experimentation, a sloped surface and forced-flow wind. The experiments were performed at multiple heat-release rates for angles from 0 to 28 degrees from the horizontal and wind speeds of 0 to 0.5 m/s. Flame geometry such as center-line flame length, flame tilt angle, and flame attachment length along the downstream surface were determined from side-view video imaging. Downstream heating was also measured through fine-wire thermocouple temperature measurements and surface total heat heat flux measurements. The measurements provided a heating profile depicting the magnitude of heating that

would be applied to unburned fuels at distances in front of a spreading fire. These profiles were compared to the flame attachment observed from imaging, and to one another. While the surface heat flux cannot be scaled to larger fires, it's relation to temperature profiles will be useful to further interpret large-scale experiments and as validation data for numerical modeling of fire behavior of the combined effects of slope and wind.

THE INFLUENCE OF WIND ON THE STRUCTURE OF INCLINED FLAMES

by

Michael Heck

Thesis submitted to the Faculty of the Graduate School of the
University of Maryland, College Park in partial fulfillment
of the requirements for the degree of
Master of Science
2020

Advisory Committee:
Professor Michael Gollner, Advisor
Dr. Torben Gumstrup
Professor Arnaud Trouve

Acknowledgments

I owe my gratitude to all of the people who made this thesis possible and to everyone who contributed to my exceptional experience as a graduate student along the way.

First and foremost I'd like to thank my advisor, Professor Michael J. Gollner for giving me this valuable opportunity to work on such a challenging project over the past two years. He has always made himself available for help and advice and there has never been an occasion where he was too busy to give me his time. Whether he was swamped with work in his office, or traveling far and wide to share his expertise, he has always made as much time for me as possible. It has been a pleasure to work with and learn from such an intelligent individual.

I would also like to thank Dr. Torben Gumstrup, as well as Dr. Mark Finney, who supported and encouraged this project from its conception to completion. They both have been a source inspiration for the experimental methods, measurement techniques, and desired outcomes for the entirety of this project. I also would not have gained valuable laboratory experience without their support. Thanks are due to them, and Dr. Arnaud Trouve for agreeing to serve on my thesis committee and for sparing their invaluable time reviewing this thesis.

I am immensely appreciative of Mahdi Tlemsani, who has been an incalculable asset in acquiring data. He has been the single greatest experimental asset for almost the entirety of my graduate career. His precision and diligence have been key to the excellence of the data in this work.

My colleagues at the University of Maryland fire lab have contributed to my graduate life in countless ways and deserve a special mention. Evan Sluder helped me assimilate into research work and contributed greatly to my understanding of what direction my work should take. Xingyu Ren has been an infinite wealth of knowledge, he has helped me set up multiple instrumentation devices, and is a sort of wizard with computational tools and equations. My interactions with Xiayou Ju, Sriram (Ram) Hariharan, Joey Dowling, Priya Garg, Lana Benny, Zhengshang Tao, and Ben Bialis have been very fruitful, as they have all exchanged words of advice and wisdom with me at some point during my graduate career.

I owe my deepest thanks to my family. My mother and father, who have always provided the most certainty and assurance in my life, support and guide me through everything with love and passion. My siblings have always been my greatest friends, and greatest rivals, and have pushed me to achieve the best for myself and others.

I would like to acknowledge financial support from the United States Department of Agriculture Forest Service, and National Science Foundation.

Table of Contents

List of Tables

List of Figures

Chapter 1: Introduction

1.1 Wildland Fire

Two of the most destructive wildland fire seasons on the record in the United States occurred in 2017 and 2018. The federal cost of suppressing fires for each year was around $3 billion, nearly triple the average suppression cost for the period of 1995 to 2010 [1], and taking up over half of the U.S. Forest Service's annual budget [1]. There are compounding factors leading to the increase in devastation from wildland fire across the western United States, but for example, "climate change has led to fire seasons that are now on average 78 days longer than in 1970" [2]. With longer fire seasons comes more opportunity for hot, dry, windy conditions that increase the risk for extreme fires. Longer seasons and an ever-growing budget for suppression has led to a decreasing effort in forest management and wildland fire research. Scientific advancements in wildland fire behavior and new methods for fire management are absolutely necessary for curbing the inflation of the budget and hazardous fire seasons that currently have no end in sight.

Wildland fire spread is typically characterized as a function of wind, fuel and slope which together make the fire triangle. Vegetative fuel has a wide range of characteristics that dictate its ignition propensity and rate of fire spread, including

fuel loading, size, shape, continuity, position, and moisture content. Weather is the most variable condition affecting wildland fire spread, encompassing changes in ambient temperature, relative humidity, atmospheric stratification, and of course wind speed and direction. Topography, i.e. aspect and slope, directly affect the rate, direction and intensity of fire spread. Geographical features of the landscape can be considered steady in time, but spatial changes can affect the fire spread rate.

Modeling wildland fire flame spread is useful for assessing risk, wildland management, and suppression operations. Current models are able to provide a simulation of wildfire spread circumstances given inputs about the fuel, weather, and topography. This information is used by community planners and incident commanders to make somewhat informed decisions about risk mitigation and asset deployment. There is a need to improve the accuracy of the output provided by these models in order to have more reliable information for strategic decisions. To do so, there needs to be a fundamental adaptation of the current wildland fire spread theory into a more physically-based understanding of the mechanics that dictate fire spread. The theory currently used in wildland fire spread models utilizes semi-empirical or empirical data correlations from the 1970s and '80s [3] [4]. Rothermel's theory gives a wildland fire rate of spread based independently on wind, slope, and fuel [3]. It does not correlate the wind and slope as two interacting features based on an understanding of their effects, instead it depicts how fast an experimental flame spreads through uniform fuel beds with and without wind and slope, independently. A new computational model would incorporate calculations based on fundamental theory of fuel ignition, heat transfer, and fluid dynamics to determine flame behav-

ior and spread rate. This work will consider the fluid dynamic effects of wind and slope on fire behavior, and the interaction of flames with the downstream surface.

Creation of more physically-based models requires measurement of flame behavior to develop a better understanding and postulate a theory. However, natural wildland fire phenomena is difficult to measure as the location, scale, and environmental conditions constantly vary. Attempting to record measurements on an active wildland fire is problematic because the fire can behave unpredictably, causing instrumentation to be in the wrong location at the wrong time. Laboratory-scale spreading fires have been historically used to represent some characteristics of large-scale fire behavior. Yet, these fires are still troublesome for precise measurements as they constantly move and require significant preparation. Instead, this study utilizes a stationary burner to consider flame behavior during a "snapshot" of a spreading fire under different conditions. Stationary fires can be observed and precisely instrumented to develop an understanding of the physical mechanisms that control their behavior [5]. Both wind and slope change the fluid dynamics of the flow field surrounding wildland fires and increase the spread rate. Fires with external forced-flow wind will deviate from typical buoyant-flow behavior, and will provide increased downstream heating. Fires on inclined slopes will begin to entrain more air from the downhill side, therefore increasing the flame contact and convective heating to the downstream fuel bed. The combination of interacting wind and slope and and its impact on mechanisms that drive flame spread rate needs to be quantified. The stationary burner will also allow for the study of gas-phase dynamics of flame spread separately from the solid-phase fuel ignition processes. Once a fully-

developed physical understanding is established, it can then be validated through measurements collected during instrumented field-scale fires.

Examining flame geometry and heating profiles ahead of a stationary flame front under various forced flow and inclined conditions will create a better understanding of how these measurement techniques are able to predict the flame behavior. Furthermore, connecting flame geometry to the characteristics of upstream heating will allow for observation of the flame geometry under mixed convection to become an accurate predictor of flame spread rate.

Chapter 2: Literature Review

2.1 Flame Spread

Flame spread can be defined as the successive ignition of fuel that allows for the propagation of flame away from the flame source. This process is said to only occur with "...some type of communication between the burning region and the nonburning fuel" [6]. This communication is in the form of a feedback loop, with the energy from burning fuel providing heat to the unburned fuel. Heated fuels begin to thermally degrade and provide volatile fuel vapors that mix with the ambient oxidizer. A spreading flame is usually a diffusion flame that is dictated by the diffusion rate of the volatile vapors with the ambient oxygen, which meet in a thin sheet in sufficient concentrations to react. The size of the flames is then dictated by the rate at which the condensed-phase fuel releases volatile vapors, and any turbulent mixing. The release of volatiles due to the thermal degradation of fuels, or pyrolysis, is controlled by the heat flux to the surface of that fuel.

For a given fire spread scenario, one or more specific modes of heat transfer will contribute heat to the surface ahead of the flame, therefore driving the forward advancement of the flaming front [6]. The fundamental equation of flame spread has been defined as an energy balance across the fuel front,

$$V_p \rho \vec{\Delta} h = \dot{q}'', \tag{2.1}$$

where V_p is the spread velocity, ρ is the density of the fuel bed, $\vec{\Delta}$h is the difference in thermal enthalpy between the burning and nonburning fuel, and $\dot{q}''$ is the heat flux to the unburned surface of the fuel [6]. If a constant ignition temperature is assumed and phase changes are neglected, a steady state flame spread equation can be formed,

$$V_p = \frac{\dot{q}''_f \delta_f}{\rho c_p (T_{ig} - T_0)}, \tag{2.2}$$

where the enthalpy is represented as the specific heat capacity $c_p \vec{\Delta} T$ [7]. The heat flux from the flame to the surface of the fuel, $\dot{q}''_f$, and the region the flame extends over the unburned fuel surface, δ_f, are the only variables that are not properties of the fuel. The heat flux to the fuel surface generally arises as the most important factor governing flame spread, and will be dictated by how much heat the flame produces and how much of that heat is perceived by the fuel. In more complex geometries, such as wind-driven flames, the flame extension length is also an important factor that is largely determined by geometry of the fuel and the ambient conditions. This parameter essentially describes the region the flame lies adjacent to the unburned fuel surface before lifting far above the fuel, diminishing heating, due to buoyancy inherent in the flame. Flame extension length therefore influences how much heat from the flame is transferred to the fuel and over what distance. Understanding downstream heating from flames under different ambient conditions, namely wind

and slope, will therefore be a primary focus of this work.

Established flame spread theory used for wildland fire spread modeling generally considers radiation as the dominant mode of flame spread, as it was thought to have provided the most pre-heating energy to the downstream fuel [3,8,9]. However, it has been found experimentally that fine fuels (∼1 mm diameter) are not able to ignite from radiation alone, as they undergo convective cooling at a rate higher than they are radiantly heated, due to their high surface area to volume ratio [10]. The convective heating and cooling process was discussed in early experimental and theoretical studies, but was not well-understood or thought to be determinant in the ignition of vegetative fuels [6, 8, 11]. Convective heating as a driving fuel ignition process was supported when experimentation found that fine particles were never able to reach ignition temperatures with high levels of radiation from a spreading fire, instead exhibiting heating in a stair-step fashion until ignition from intermittent bursts of heated gases impinging on particles ahead of the fire front [12]. Ignition of fine fuels is important as it is the primary mode of spread for forward-spreading fires. The progression of evidence has revealed that considering only radiation from a flame front will not accurately capture the ignition process of fine fuels.

Numerically modeling individual fuel particle ignition and small scale intermittent heating processes may be possible at the the laboratory scale modeling level. However, Finney [12] states that "...models intended for the large domains of actual wildfires... must use coarser resolutions and parameterize the convective heat transfer and ignition processes based on careful comparison with experimental data." In order to parameterize the heat transfer for fire spread experiments, research has

been largely focused on measuring the heat perceived at distances ahead of the flame front. This is typically done with a spreading flame [13–15], which involves solid-phase fuel pyrolysis. Some studies consider heat flux measurements in front of a stationary burner [16, 17], allowing for analysis of the gas-phase decoupled from the solid-phase.

A stationary burner allows for a long-duration test in which a large sample size of data can be taken with greater control over experimental variables, like the heat release rate, HRR. Stationary flames allow for the capture of consistent measures of flame geometry and downstream heating that are difficult to measure in a spreading fire. Flame structures like buoyant instabilities and intermittent forward pulsations are observed in stationary burners and replicate gas-phase effects seen in spreading fires through uniform fuel beds [18]. Narrowing in on the effects that wind and slope have on this stationary small scale flame will provide a basis for how large scale and spreading flames are affected by similar external flow fields.

The majority of previous studies are concerned with downstream heating measurements for a varying angle of fuel orientation or a varying external forced flow, with only some of the studies attempting to examine both variables in conjunction. Reviewing the conclusions drawn from the single-variable studies will assist in formulating the methods for exploring the combined affects of wind and slope.

2.2 Inclined Fires

In the wildland environment, a rapid increase in wildland fire spread rate is observed when fires spread up a slope, driven especially due to the flame attaching to the surface ahead of the flame [19]. Morandini et al [20] conducted observational studies of the fluid dynamics surrounding flame spread up an inclined surface. It was determined that the local wind surrounding a flame is typically towards the flame as it entrains air, but as the incline increases and the flame attaches to the surface the local wind on the uphill side is inverted away from the flame [20]. Congruently, it was observed that significant convective heating of fuels on the uphill side occurs as the local wind begins to blow away from the fire [20]. Dold and Zinoviev also studied how spread rate, and a dramatic increase in spread rate under steep slopes, were driven. They found flame attachment to the vegetation surface ahead of the fire led to an increase in the spread rate [15].

The 1987 disaster at King's Cross railway station saw a rapid increase in fire spread rate up a wooden escalator take the lives of dozens of people. Following the disaster, several sets of experiments were undertaken to investigate the effects of flame spread up an inclined channel [5, 21–23]. The studies initially confirmed that fire spread was faster up a steeper sloped surface. Atkinson et al [5] utilized a stationary gas burner on an inclined trench at varying angles of inclination. It was found that at angles less than 24 degrees from the horizontal the flow was dominated by buoyancy, and at angles greater than 24 degrees the buoyant flow came into contact with the surface downstream of the burner. Smith [24] found a

qualitative measurement of the flame angle tilted away from the vertical, ϕ_{vert}, in relation to the angle of the inclined trench, θ,

$$\phi_{vert} = 2\theta, \tag{2.3}$$

that described the buoyany plume's behavior in relation to the incline of the surface. The consensus of studies motivated by the King's Cross fire was that flame behavior and spread rate up an inclined slope changed drastically after a certain angle of incline was reached. The changed behavior resulted from air entrained by the fire coming only from the downhill side of the flame. As a result, flames get pushed close to the fuel surface, and an exponential increase in fire spread rate occurs. This became known as the "trench effect", also known as flame attachment. The critical angle at which flames exhibited this behavior was much less when the flames were in a channel, or an inclined surface with sidewalls, such as the escalator in the King's Cross fire [22].

More recent studies considered flame spread over a flat inclined surface without sidewalls for a range of angles. Gollner et al considered burning rate and spread rate over PMMA samples at different angles of incline. Fig. 2.1 compares the spread rates found over similar experiments involving inclined PMMA samples. Gollner et al also considered heat flux estimates to the surface and the distance that the tip of the flame was from the surface, or the "standoff distance". An assumed straight line from the flame source and that flame tip creates an angle that the flame is leaning away from the vertical. This angle is indicative of how much the flame is exhibiting

the "trench effect" behavior, as the flame is going against normal vertical buoyancy behavior to lean closer to the fuel surface. Non-steady effects in the burning rate and spread rate were found to be significant, due to the non-steady nature of a spreading fire. Non-symmetric "necking" effects due to air entrainment from the edge of the surface were observed that created quantitative differences in heat flux measurements. Sidewalls work for eliminating this 3D necking effect by removing air entrainment from the sides of the experimental surface.

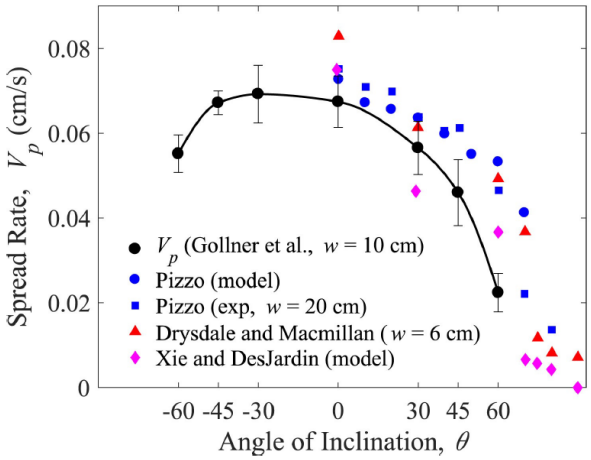

Figure 2.1: Reported flame-spread rates against angle of inclination for small scale fires are shown from Gollner et al [13], Pizzo et al. [25], Drysdale and Macmillan [22], and Xie and DesJardin [26]. Figure from [27].

2.3 Wind-Driven Flames

External flow fields have an impact on flame spread similar to inclination. Incoming wind competes with buoyant forces from the flame and the flow begins to

attach to the surface. This differs from the inclined scenario in that the flow in the forced-flow case is no longer driven by the fire itself. As flames are forced closer to the fuel surface by increasing wind speeds, a rise in the preheating of unburned fuels causes more rapid rates of flame spread. For smaller-scale flame spread experiments, the flame-spread rate increases nearly linearly with increasing flow velocity [27, 28]. This is unlike the inclined scenario, where flame spread rates increase dramatically after a critical inclination angle [22, 27]. Tang et al [16] measured total heat flux profiles downstream of a stationary line burner in a wind-driven scenario. The flame behaved similar to the inclined scenario, where the flame lifted away from the surface under low velocity conditions, and attached to the downstream surface under high wind speeds [16]. This study also found that the peak heat flux measurement during tests could be correlated to where the Richardson number

$$Ri = \frac{g\beta\left(T_F - T_\infty\right)x}{U^2}, \tag{2.4}$$

is equal to unity, and the heat flux and flame lift off measurements are liearly correlated [16]. At unity, or $Ri = 1$, the buoyant forces from the heat released by the flame are equal to the momentum forces from the oncoming wind, and the flame lifts off the surface [16].

A different study by Tang et al considered the intermittent extension of flames in wind-driven fires and found a correlation that approximately related the flame attachment length to competing buoyancy and momentum forces, which were approximated with the center-line flame length and wind speed [18]. These findings work

for purely forced-flow transition, however for transition from buoyant to momentum-driven flames involving both wind and slope, a theory or correlation does not yet exist that matches upstream heating from flames found experimentally.

Mao et al [29] considered a theoretical approach to analyzing the competing affects of forced-flow and buoyancy driven flame spread. Their work formulated a mixed convection parameter

$$(Re_x^n + Gr_x^m)^{1/2n} \tag{2.5}$$

that scales their experimental variables, and a mixed convection ratio

$$(Gr_x^m / Re_x^n)^{1/2} \tag{2.6}$$

that indicates whether the boundary layer more nearly represents forced or free convection. The idea of competing forces of buoyancy and forced flow is intended to apply for fires with nearly any external conditions, including wind and slope. The boundary layer created by these competing forces directly affects the heating profile downstream of the flame. This theoretical solution is highly simplified and cannot account for any turbulent effects inherent in buoyancy flows from fire. The scientific community has not been able to validate a working theory for the combined effects of wind and incline on the boundary layer and downstream heating from a spreading, or stationary, flame. Detecting the downstream heating profile has been done with both thermocouples and heat flux gauges in the past, both of which will be discussed further.

2.4 Measurement Techniques

Studies considering the measurement of heat flux ahead of both spreading and stationary fires in sloped [30, 31] and forced-flow configurations [28, 32] have been conducted in the past. Due to the complexity of the flame spread process, most previous work simplifies dependence of the heat flux on distance ahead of the pyrolysis zone as a constant [33, 34] or as an exponential function of downstream distance [13]. Markstein and de Ris postulized the forward heat flux ahead of a pyrolysis front as an exponential decay function of downstream distance [35]. This function is represented as

$$\dot{q}''_f(x) = A(x/x_p)^n \tag{2.7}$$

where x is the downstream distance from the edge of the fuel, x_p, is the pyrolysis length, and A and n are constants that are fit to the data. Gollner et al used the same relationship, with values for n to be between -5 and -7, for flames on top of inclined surfaces [13]. No values for this exponential decay function were found in the literature for forced-flow flames.

Previous studies have confirmed that both an inclined fire and a wind-driven fire will have competing effects of buoyant and forced flows from the external conditions. Studies have individually described either flame attachment on inclined surfaces [10,11] or wind-driven configurations [8,18,19], but few have addressed both in conjunction.

Thermocouples measure gas temperature and have often been used for mea-

suring high-temperature turbulent flames [36–38]. However, when making thermocouple measurements in a highly-fluctuating fire corrections must be made for the thermal inertia of the thermocouple bead. A dual-thermocouple technique can be used to correct for the frequency response of thermocouples through use of a first-order time constant coefficient [39]. However, this technique was originally extremely difficult as it relied on the local velocity [40]. A similar technique relied on an assumption of fixed thermocouple bead size, which can change under sooty conditions and cause large errors [41]. The dual-thermocouple technique has been improved on so the time constant can be estimated without an assumed bead diameter, making it useful for applications in sooty flames [39, 42, 43].

In wildland fire studies thermocouples somewhat mimic the realistic scenario of fine vegetative fuels just above the surface. Studies have analyzed the flame front and heating downstream of a spreading fire using thermocouples [17,44]. Finney [44] empirically found an exponential decay of the temperature of the hot gases ahead of the flame front that may be useful in describing the convective heating applied to fine fuels ahead of a spreading fire. These studies did not correct for soot accumulation on the thermocouples, and the systemic uncertainties previously discussed could potentially spread across multiple experimental studies, leading to a broad misunderstanding of the actual heat being perceived upstream of the fire front. There is also the intrinsic unsteady nature of a fire. Even with a stationary burner the flame will have buoyant instabilities that will translate into highly variable thermocouple readings. This study aims to utilize a thermocouple measurement method to make corrections for true gas temperature in order to negate thermocouple bead size and

re-radiation effects. This will be done in conjunction with collecting heat flux gauge measurements and comparing the two techniques for measuring heat profiles ahead of the flame front in order to determine if they provide agreeable results.

Chapter 3: Experimental Methodology

3.1 Overview

The independent effects of wind and slope on flame spread through vegetative fuels are well studied in the literature. However, few studies have incorporated the combined effects of wind and slope on fire spread. Relationships that quantify flame attachment and downstream heating profiles, which drive forward fire spread, are notably absent. In this study, three measurement techniques are utilized to investigate flame behavior from a small-scale forced-flow inclined gaseous burner with controlled ambient flow, heat-release, and slope to start to understand the relationship between these quantities and forward flame heating.

Experiments were conducted on a small-scale tilt table that allowed for variation of the incline of the surface and a modular detachable wind tunnel that provided variable wind speed. A gaseous burner embedded into the surface provides variable fires sizes. From this setup, three variable conditions provide the basis for the analysis of fire behavior. Side-view imaging, downstream total heat flux gauges, and traversed fine-wire thermocouples were used to independently collect information on flame characteristics and downstream heat transfer which are later compared. This chapter provides a detailed description of the experimental setup and data

collection processes.

3.2 Tilt Table Apparatus

The experimental apparatus in Fig. 3.1 was custom-built to study the combined effects of wind and slope on the flame behavior and downstream heating. The experiment used a gaseous propane sand burner to provide a steady, uniform flame that is always in the laminar or laminar unsteady regime. It provides for long-duration sampling with greater control and de-coupling from other experiment parameters, allowing for more readily available and repeatable measurements. Propane was used for the gaseous fuel because it is highly available, and can be readily scaled-up for future large-scale studies. Propane diffusion flames also have similar temperatures and sooting characteristics as wildland fire flames. Stationary, gaseous sand burners have been used in previous fire spread studies [16, 17] which allows for comparison of this experiment to previous results. The burner used here had an outlet area of 5 cm $\times$ 25 cm. To uniformly distribute the gas at the outlet of the burner the top layer of sand was placed on top of a fine metal mesh. This arrangement produced a plenum beneath the mesh that evenly distributes the gas to the outlet of the burner, resulting in a uniform flame. An Alicat MCP-10SLPM-D/5M flow controller provided flow rates of 2 to 7 slpm of propane that was injected into the bottom of the burner. This allowed for accurate and steady control of the size of the fire known as heat-release rate, or HRR.

A Beacon Industries BBTT-5-36 bench top pneumatic tilting table was used

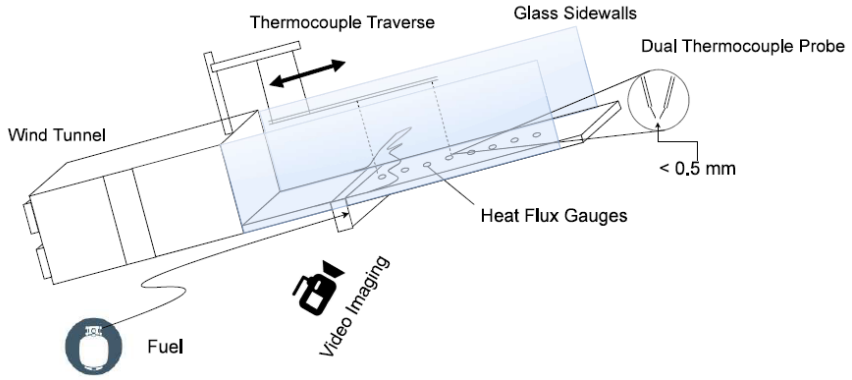

Figure 3.1: Diagram showing the experimental setup and instrumentation. Objects shown are supported by the tilting table and aluminum frame.

to precisely vary the inclination of the entire test apparatus. This test apparatus had a 30 cm $\times$ 120 cm top surface of 12.5 mm thick ceramic insulation board (Superwool 607 Board) that was added flush with the top outlet of the burner. 80/20 aluminum struts were used to support the test surface, walls and diagnostics on the tilt table. The insulation board was installed in 2 pieces around the front and back of the burner and provided a relatively adiabatic experimental surface that would not interfere with the flame's behavior. At both edges of the insulation board surface there is a glass panel extending 30 cm above the surface. This glass panel provides a boundary that simulates a nearly 2-D fire that extends infinitely in a line in either direction. This infinite line fire simulation negates the necking effects that air entrainment from the side of the flame would have on the flame behavior. The fuel bed and instrumentation are shown in Fig. 3.2 with dimensions. A large spreading fire can also be assumed to be a 2-D line fire, therefore it is reasonable to emulate such a flame with sidewalls. The sidewalls also increase the so-called

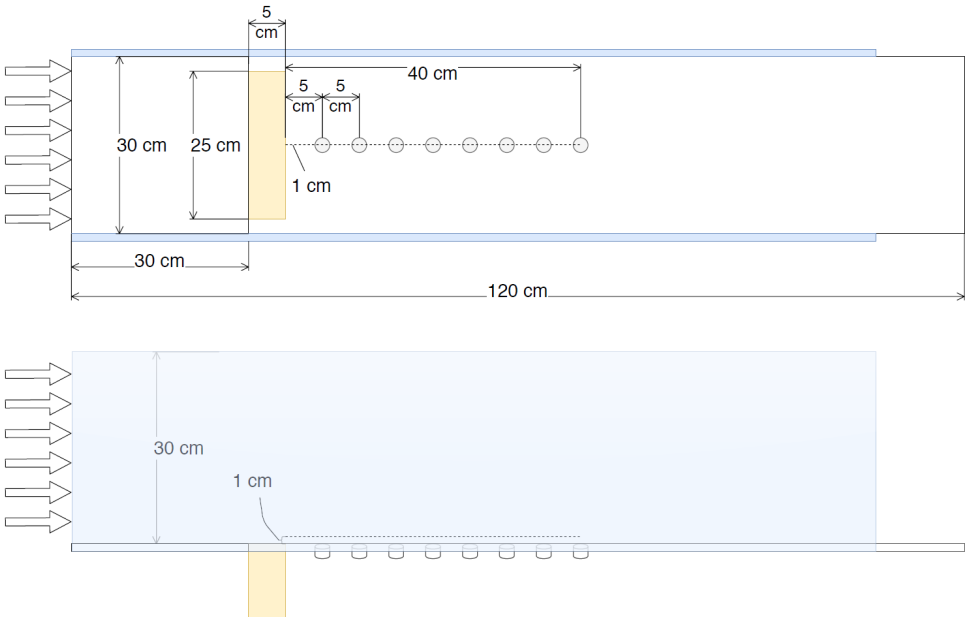

Figure 3.2: Diagram showing the experimental surface and instrumentation with dimensions, in a top view and side view configuration. Objects shown are the insulation board fuel bed, sand burner, glass sidewalls, and heat flux gauge and thermocouple measurement locations.

19 trench effect [21–24] that increases the attachment behavior of the flame. There is a 2.5 cm gap between either side of the burner and the edge of the insulation board surface and glass sidewalls. The small gap prevents the flame from directly interacting with this glass wall and interfering with flame behavior. The tilt table setup is shown in Fig. 3.3 without any instrumentation, and an image of the fire emanating from the stationary burner is shown in Fig. 3.4.

The modular wind tunnel was designed and built following multiple studies for similarly constructed wind tunnels [45, 46]. The tunnel is mounted to the apparatus so that it varies with the same angle as the rest of the experimental setup, providing wind that is parallel to the experimental surface. The wind tunnel is a push-type

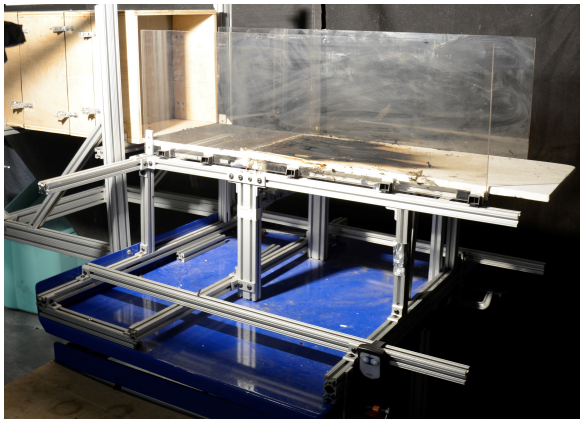

Figure 3.3: Image of the experimental setup, stripped of any instrumentation. The blue tilting table holds the insulation board surface with embedded burner, girdled by two glass side walls, with the attached modular wind tunnel in the rear.

wind generation method that is upstream of the flame. This wooden wind tunnel is best placed upstream so that it does not catch fire during experimentation. The wind tunnel outlet is 30 cm $\times$ 30 cm, and aligns with the 30 cm width of the insulation board and the 30 cm height of the glass panels. The wind tunnel is framed with 1.25 cm thick wood paneling that contains a series of hexagonal flow straighteners and fine wire meshes. A honeycomb mesh was used to dampen swirl effects and straighten the velocity variations, and mesh screens were used to break up larger turbulent eddies [47]. The open outlet of the tunnel is approximately 15 cm from the edge of the nearest mesh screen. Air is pushed through these meshes after being drawn into the constructed box with four powered computer cooling fans. The computer fans have a 1.05 m^3/min capacity and are supplied by a variable Drok DC motor controller allowing a range of 0.2 to 0.5 m/s air speed. These air flows were tested using a hot wire anemometer (HWA) that confirmed that these air flows were

Figure 3.4: Image of the experimental flame under some combination of forced flow and incline that shows the uniformity of the flame structures. It is apparent that the flame does not have significant edge effects.

steady and uniform across the outlet of the wind tunnel, which will be discussed in the next section of this chapter. It is important to note that the wind tunnel provides relatively low wind speeds. Considering the low wind speeds and short distance between the wind tunnel and test section an estimate of the local Reynolds number ($Re \sim 0.5 \times 10^4 - 1.5 \times 10^4$) falls far below transition to turbulence for flow over a flat plate (5×10^5). Even with changes from buoyancy generated from the fire, observed behavior of the flame suggests that flames remain in a laminar or laminar unsteady flow regime, without ever fully entering a turbulent flow regime.

In order to collect data in an efficient manner, a limited series of tests was conducted for each measurement technique. Tables of all of the tests run and their corresponding conditions are available in Table 3.1. The side-view imaging had

the most tests, as it was the least involved measurement technique and provided the most information about flame characteristics. The standard set of tests were conducted at angles above and below where the expected attachment location would be in order to produce fully-developed data curves. The tests were conducted at three different fire sizes and all possible wind speeds. This was repeated three times to ensure the results were reproducible and estimate the error involved in measurement. To be sure that the results for the selected angles and heat-release rates were producing suitable results, separate series of tests were conducted at odd-numbered angles, higher angles, and odd-numbered heat-release rates. These series of tests are all outlined in Table 3.1. The heat flux gauge data collection had a more limited range of tests that were conducted, and they were only conducted twice. The thermocouple data had the highest sampling rate, most data points, and the most arduous data collection and post-processing methods. Therefore, the least amount of thermocouple data was collected, but enough to compare to the other measurement techniques. The series of thermocouple data collection tests were only repeated once.

3.3 Hot Wire Anemometer

It is desirable for the wind profile coming from the outlet of the wind tunnel to be as uniform across the experimental cross-section as possible, and steady in time across this profile. The wind tunnel speeds were tested first across the entire opening of the wind tunnel, with the Kanomax Anemomaster-LITE Model 6006-0E.

This hand-held anemometer, HHA, has a resolution of 0.01 m/s, and an accuracy of ±5% of the reading. The HHA was used to determine the power input to the fans to reach desired wind speeds of 0.2 m/s, 0.3 m/s, 0.4 m/s, 0.5 m/s. These wind speeds were tested with the HHA and found to be the same for all points of the outlet of the wind tunnel, and relatively steady. The hot wire anemometer probe, HWA, is a constant temperature Dantec Dynamics 55P16 single-wire probe capable of 5000 Hz readings and was calibrated using these known wind speeds. The output voltage of the anemometer at each known wind speed was turned into a 4th-degree polynomial calibration curve to give an accurate wind reading for any future voltage output. The HWA was then traversed vertically and horizontally across the opening of the wind tunnel and 15 seconds of data was recorded at 18 locations for each orientation. The results at each wind speed are shown in Fig. 3.5 and Fig. 3.6 for vertical and horizontal traversing, respectively.

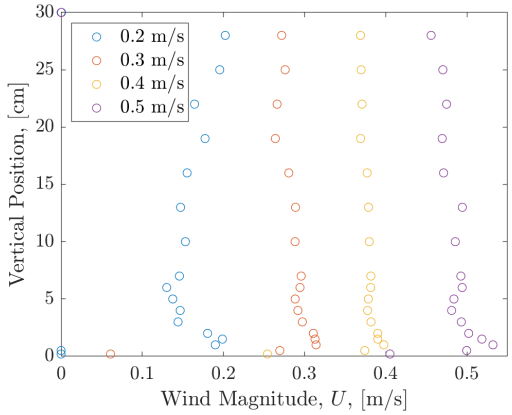

Figure 3.5: The recorded wind speeds at various locations across the vertical span of the outlet of the wind tunnel.

The wind speeds could not be tested live during the experimentation because

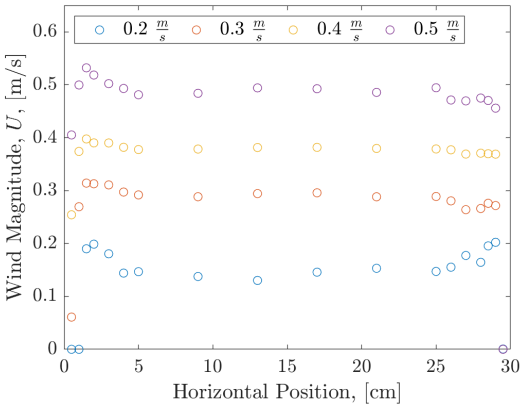

Figure 3.6: The recorded wind speeds at various locations across the horizontal span of the outlet of the wind tunnel.

heat from the flame heavily affects hot wire anemometer readings, and could potentially damage them.

3.4 Side-View Imaging

The first method for measuring the flame response to varying conditions was side-view imaging. The process provides a consistent procedure that translates into dependable flame geometry data. Through a variety of image processing methods, basic measurements of the flame can be taken for the wide variety of conditions, and compared to each other, as well as compared to the other measurement techniques.

The camera used for video data collection was a Nikon D7100, capable of 1080p high-definition video with a frame rate of 60 Hz. It was setup with the 105mm Nikon DX AF-S NIKKOR lens exactly 87 cm from the face of the glass nearest the camera. The camera's settings were adjusted to 640 ISO, F4 shutter

speed, and 640 aperture. These settings only allowed 720p HD video, but were kept consistent throughout the entirety of the data collection process. This allowed for dependable image collection that will render the later image thresholding process effective. The camera was originally setup on a tripod that was raised and tilted to become in-plane with the surface each time the tilt table angle was changed. To ensure the camera was perfectly in-plane with the surface, a measuring ruler was placed along the center-line of the burner and the camera was adjusted until just the bottom edge of the ruler was visible, and no amount of the surface was visible, as shown in Fig. 3.7 . The camera was also centered on the front edge of the burner, with zoom set to 18 mm, and manually focused on the ruler. This ensured that the camera's point of focus was on the the approximate center of where the flame would be at all times.

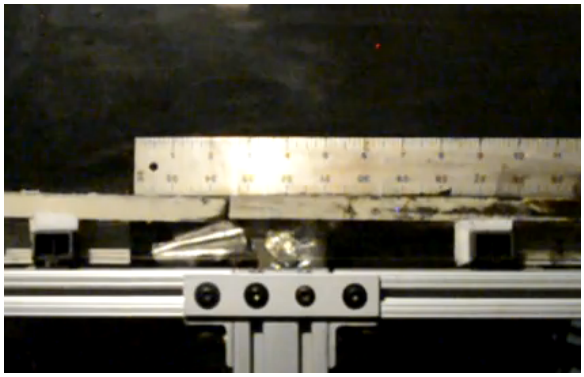

Figure 3.7: Side-view image the ruler used to level the camera with the burner.

This process of changing the camera positioning each time the tilt table angle was changed provided entirely uniform imaging conditions, but it was highly time consuming. In order to streamline the data collection process, the camera was

mounted to the tilt table so that it would move with the tilt table and always be in the correct position. The same setup process as with the tripod was undergone, with the camera lens 87 cm from the glass, and the bottom edge of the ruler made visible and in-focus. This process was repeated periodically throughout testing to ensure the camera was still in position, and was always in-plane regardless of the angle of the tilt table, which it was. This attached camera setup was used for collection of all of the imaging data presented in this study, and a 3D rendering of the experimental setup positioned above the tilting apparatus is shown in Fig. 3.8.

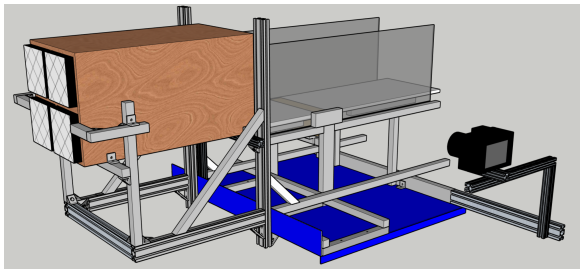

Figure 3.8: 3-D rendering of the table-top experimental setup. The modular wind tunnel is to the left side of the glass sidewalls that encapsulate the burner and experimental surface. The attached camera is to the right and rotates as the entire aluminum-framed setup tilts as one unit.

Imaging was performed for a series of fire test conditions. For each test, the flame was lit and allowed to burn for a minimum of 30 seconds, ensuring a steady state was achieved. Video was then recorded for approximately 1 minute, then the next test was conducted. The ventilation hood was turned off and the laboratory doors were kept closed in order to minimize ambient air flows. After a number of tests, experimentation was paused so the ventilation hood could be run to clear the room. The room was then allowed to settle for 5 minutes before testing resumed.

The clear glass sidewalls allowed for clear visualization of the flame. However, after a number of tests they would become covered in soot, and testing would need to be paused in order for the glass to be cleaned. Hysteresis effects, defined as lagging of the flame behavior, were accounted for through a waiting period of around 1 minute after test conditions were changed, which was found to provide enough time for the new flame conditions to become fully steady. No-wind tests were conducted separately from tests including wind, as the wind tunnel needed to be removed in order to allow for unobstructed air entrainment from the upstream side.

The video camera setup process allowed for a consistent field of view and a reference point for pixel measurement. The ruler provided a reference to a known length scale placed at the center of the flame which will be used to measure the flame dimensions. First however, images needed to be extracted from the raw video imaging data collected during experimentation.

Raw video was converted from the smaller-sized .MOV file into a larger .AVI file. This was done with the Windows 10 PowerShell window and a short string of code for each video file. This allowed for the .AVI version of the video to be imported into the MATLAB computer program. In MATLAB, each frame of the video was extracted as an individual image. A single 1 minute test at a frame rate of 60 Hz provided about 600 individual images. These images were averaged together to get a single image that represented the average flame location over 1 minute. This image was converted to a black and white image, and a threshold of 60% of the gray-scale values for each pixel was used to determine where the flame was present 60% of the time. This created a consistent process for determining a characteristic

flame shape for flames that puffed. When the flame puffs it would be present in one frame and not in the next, requiring an averaging of the image to get the actual shape of the flame over time. This threshold was used to create a binary image of where the flame was present. Reference images that were taken intermittently during testing to check the camera alignment also provided an image that allowed for location and measurement of the burner. The edges and center of the burner are visible in Fig. 3.9. This measurement of the burner provided a pixel value for the known 5 cm width of the burner. This could then be used as a conversion ratio for any pixel measurement taken of the flame. To characterize the flame, measurements of the thresholded flame shape were taken for each test scenario.

Visually, flame attachment is apparent from where the processed flame outline is on the same level as the burner. Flame attachment length to the downstream surface, L_a, is quantified as the distance from the front of the burner to where the flame ceases to be present at a height of 2 mm (5 pixels) above the surface of the burner. The center-line flame length, L_f, is taken as the assumed straight-line distance from the center of the burner to the flame tip. The flame tip is determined by finding the image pixel of the flame with the greatest distance from the center of the burner. Flame angle, ϕ, is taken as the angle above the in-plane surface of the straight line from the center of the burner to the flame tip. The flame angle is not taken as the center-line flame tilt from the vertical, as previously defined by Albini [48]. Flame height, H_f, is taken as the distance from the flame tip to the surface of the burner. This is taken as the flame height regardless of whether it is the tallest point of the flame from the surface. For most conditions the flame tip is

just about the highest point, but for laminar flame conditions the body of the flame can actually farther from the surface than the tip of the flame. These measurements were taken for an image comprised of an average of about 600 frames, or 1 minute of video. An exemplary averaged, processed image with measurements is shown in Fig. 3.9.

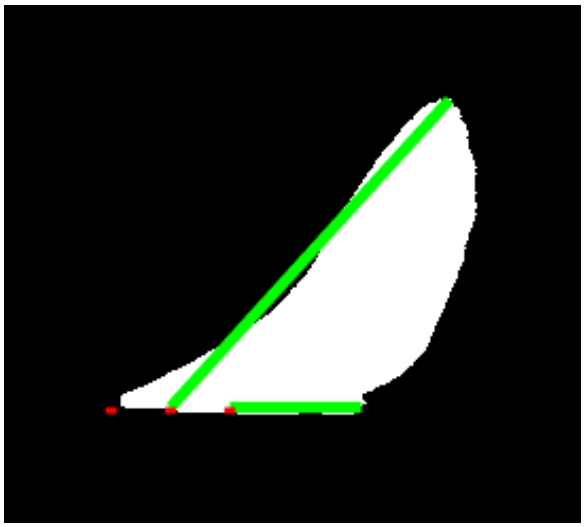

Figure 3.9: Side-view image of a representative flame with green lines shown for flame length and attachment lengths measured, as well as small red markings for the location of the center and edges of the gas burner.

3.5 Heat Flux Gauge Measurements

Heat fluxes to the surface downstream of the burner was measured using two Hukseflux SBG01 water-cooled total heat flux gauges. These gauges measure the convective and radiative heat transfer from the flame incident to the surface that extends beyond the burner. Before testing, the gauges are cleaned and painted

with a fresh coat of MEDTHERM high temperature optical black coating, with an absorptance of 0.95. The freshly-painted gauge is calibrated to a NIST-traceable reference heat flux gauge beneath a radiant cone heater. The gauges are then placed flush with the surface of the ceramic insulation in holes cut through the insulation in 5 cm intervals, starting 5 cm beyond the burner. Two gauges allows for two measurements to be taken, then the gauges are moved to two different spots to record different measurements under the same set of conditions. The holes that remained in the experimental surface were plugged with circular ceramic fiberboard insulation cutouts that fit flush with surface and the outline of the hole in the surface. This allowed for easy movement of the gauges without air from below the surface interfering with the flame and downstream heating. The heat flux gauge data is taken at a rate of 50 Hz, for about 1 min, at 8 different positions along the experimental surface. Therefore, the same set of test conditions had to be completed 4 times, with the gauges moved each time, to complete an entire test series.

Heat flux gauge data collection was complicated by the accumulation of soot and even condensation on the surface of the gauge. The gauge is water-cooled from the colder-water tap, therefore a large temperature gradient existed between the gauge and the surrounding hot gases of combustion. This led to a heavy soot accumulation from the thermophoresis effect. It also caused water vapor from the flame to accumulate on the cold surface. This was initially concerning, however the condensation issue was solved by pausing between tests and if condensation was present, gently cleaning the surface with a compressed air canister. The soot issue was found to be not an issue after it was recalibrated with a heavily sooty surface

and the calibration showed that the readings did not vary more than 1.6% from the calibration with a freshly painted gauge. The re-painting and recalibration process was still continued at the same interval after a completion of a set of tests. The re-calibration process always results in different calibration coefficients because of the nature of re-painting. However, because the calibration was completed in an identical manner with the same reference gauge, it is expected that the readings are consistent between sets of tests.

Two series of heat flux gauge test cases were conducted for repetition. Both series and their corresponding conditions are outlined in Table 3.1. During the first series, the gauges were spaced 5 cm apart, and a set of 45 test conditions were conducted. The gauges were then cleaned, painted, calibrated, and moved 10 cm downstream for the tests to be run again with different heat flux data recordings.

During the second heat flux test series, the gauges were placed initially at locations of 5 and 25 cm downstream of the burner. After running the set of 44 tests, the gauges were each moved 5 cm downstream. After repeating this process 4 times, heat flux gauge data was collected at each of the 8 locations.

3.6 Thermocouple Temperature Measurements

The third data collection technique involved fine-wire thermocouples that were traversed across the surface beyond the burner to measure temperatures near the downstream surface for comparison to diagnostics taken at field scale and similarly instrumented burns at large-scale. The R-type thermocouples used had wire diam-

eters of 25 μ (0.001 inch) and 75 μ (0.003 inch). The thermocouples wires were purchased with a pre-manufactured thermocouple bead from OMEGA along with ceramic thermocouple insulators, TRX164116-6, with 1.575 mm outside diameter and 0.406 mm inside diameter, that have two holes and are about 15 cm in length. The thermocouple wires are gently fed down the ceramic tube and connected to an extension wire connection on the other end. One thermocouple of each size are taken and conjoined at the connectors and along the ceramic tubing in a way that allows the resulting two thermocouple beads to be within 0.5 mm of each other. The two thermocouples were assumed to be in the exact same position, receiving the same amount of heating from ambient gases. This allowed for the two temperature measurements from two differently sized thermocouples to be corrected for a true-gas temperature using the time constant method utilized by [39,43] and developed by [42]. Four thermocouples were used in all, two side-by-side, and another two placed 20 cm downstream. This setup is shown in Fig 2, with the thermocouples placed at a distance of 1 cm above the surface from above. The 1 cm height is an approximate height of a laminar boundary layer flame downstream of the burner. The thermocouples were then traversed a distance of 20 cm at intervals of 1 cm. This gives a total of 40 thermocouple readings at 1 cm increments. This allowed for the best resolution of data collection. The data was collected for 10 second time intervals at each position, at a rate of 5,000 Hz.

To insert the thermocouple beads to a height of just 1 cm above the surface and 20 cm apart, a system of metal arms was constructed above the experimental surface. The arms allowed the thermocouple extension wires and junction to be

attached and then covered with aluminum tape and aluminum foil to shield them from the heat of the fire. This setup is visible in Fig. 3.10, along with the traverse apparatus. This created stable and adjustable instrumentation, however on several occasions the heat from the flame melted the junctions or extension wires of the thermocouples. This meant that the flame had to be stopped every few positions to allow the thermocouple arms to cool, especially when the flame was in a plume mode. Stopping the thermocouple data collection periodically translates to inconsistent data collection. To correct for this, the data was collected continuously until the thermocouple arm began touching the plume, then the experimentation was stopped every 3 tests. The flame was reignited after a period of cooling, and the flame was allowed to steady for at least 30 seconds, and up to 1 minute. This process was continued until the thermocouple arm ceased touching the flame.

The thermocouples were affected by soot from the propane flame. It would collect on the thermocouple wires, especially in the unsteady diffusion zone, or the distance at least 5 cm from the outlet of the burner, under non-laminar flame conditions. The simple way of dealing with this was to traverse the thermocouples through flame while under laminar flame conditions, and it would quickly burn off the soot, at which point the data collection process resumed.

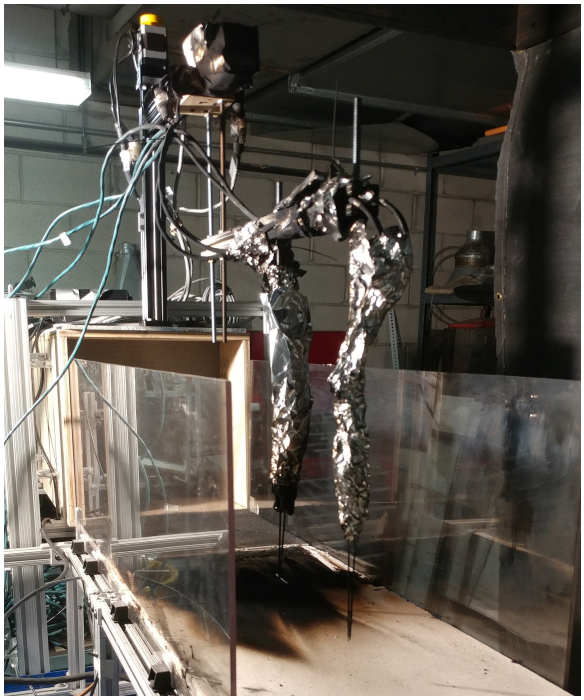

Figure 3.10: The dual thermocouple probe setup is shown with the traversing mechanism. The thermocouple extension wires are wrapped in aluminum tape to protect them from the heat of the flame, but the thermocouple wires and ceramic tubing are entirely exposed.

Table 3.1: Overview of the range of conditions for the side-view imaging test series case.

Test Series	Angles	HRR	Wind
Standard Imaging (x3)	0, 6, 10 12, 14	2.8, 5.7, 8.5	0, 0.2, 0.3, 0.4, 0.5
Imaging: Extra Angles	0, 1, 3, 5, 7, 8, 9, 11, 13, 15, 17, 19	2.8, 5.7, 8.5	0, 0.2, 0.3, 0.4, 0.5
Imaging: High Angles	16, 18, 20, 24, 28	2.8, 5.7, 8.5	0, 0.2, 0.3, 0.4, 0.5
Imaging: Extra HRR	0, 6, 10 12, 14	4.3, 7.1, 9.9	0, 0.2, 0.3, 0.4, 0.5
Heat Flux Series 1	10, 12, 14	2.8, 5.7, 8.5	0, 0.2, 0.3, 0.4, 0.5
Heat Flux Series 2	0, 6, 10, 12, 14, 16, 18, 24	2.8, 5.7, 8.5	0.2, 0.3, 0.4, 0.5
Thermocouple	0, 6, 10, 12, 14, 16, 18, 20	2.8, 5.7, 8.5	0.2, 0.3, 0.4, 0.5

Chapter 4: Results and Discussion

4.1 Overview

This study has independent variables that imitate various conditions in a wildland fire, such as; forced-flow wind speed, angle of incline, and HRR. Measurements of the flame from side-view imaging produced dependent variables such as flame length, angle, height, and attachment length. These dependent variables were correlated with the independent variables to reveal trends in fire behavior. These trends, particularly those relating to flame attachment, are useful for making predictions about how a fire interacts with its environment to drive flame spread.

Data collection from heat flux gauges and thermocouples under the same independent conditions provided information about downstream heating from flames. The profile of heating downstream can indicate if the flame is attached to the surface. Flame attachment criteria is defined for each measurement technique, and the resulting attachment length for each technique can be extracted.

4.2 Imaging

Side-view imaging was recorded under a wide variety of conditions. In Fig. 4.1 the apparent effects of the external conditions on the flame behavior can be readily observed. Both the incline and the wind have an effect on the shape of the flame, tilting it towards the downstream surface, while increases in HRR increase buoyant forces lifting the flame towards the vertical.

From 4.1i to 4.1ii the effect of incline is apparent as the flame is in contact with much more of the surface. From 4.1ii to 4.1iii the effect of wind is apparent as the flame that is already in contact with the surface takes on a boundary layer shape and does not appear to lift off from the surface at all. From 4.1iii to 4.1iv the effect of HRR increases the buoyant force, and the flame is able to lift away from the surface.

The processed, side-view images of the flame allowed for consistent flame geometry measurements to be taken for each experiment. These measurements can be compared to the independent variables to describe flame behavior under given external conditions. The different flame geometries can also be compared to one another to analyze how the flame's behavior affects attachment to the surface.

The images can also be qualitatively analyzed to obtain preliminary results for the inclination required to achieve downstream heating sufficient for flames to spread through different fuel beds. Fig. 4.2 shows the flame geometry at angles of incline of 0, 6, 10, 12, 14, 16, and 18 degrees and at wind speeds of 0 m/s, 0.2 m/s, 0.3 m/s, 0.4 m/s, and 0.5 m/s. An outline of the range of test conditions can be

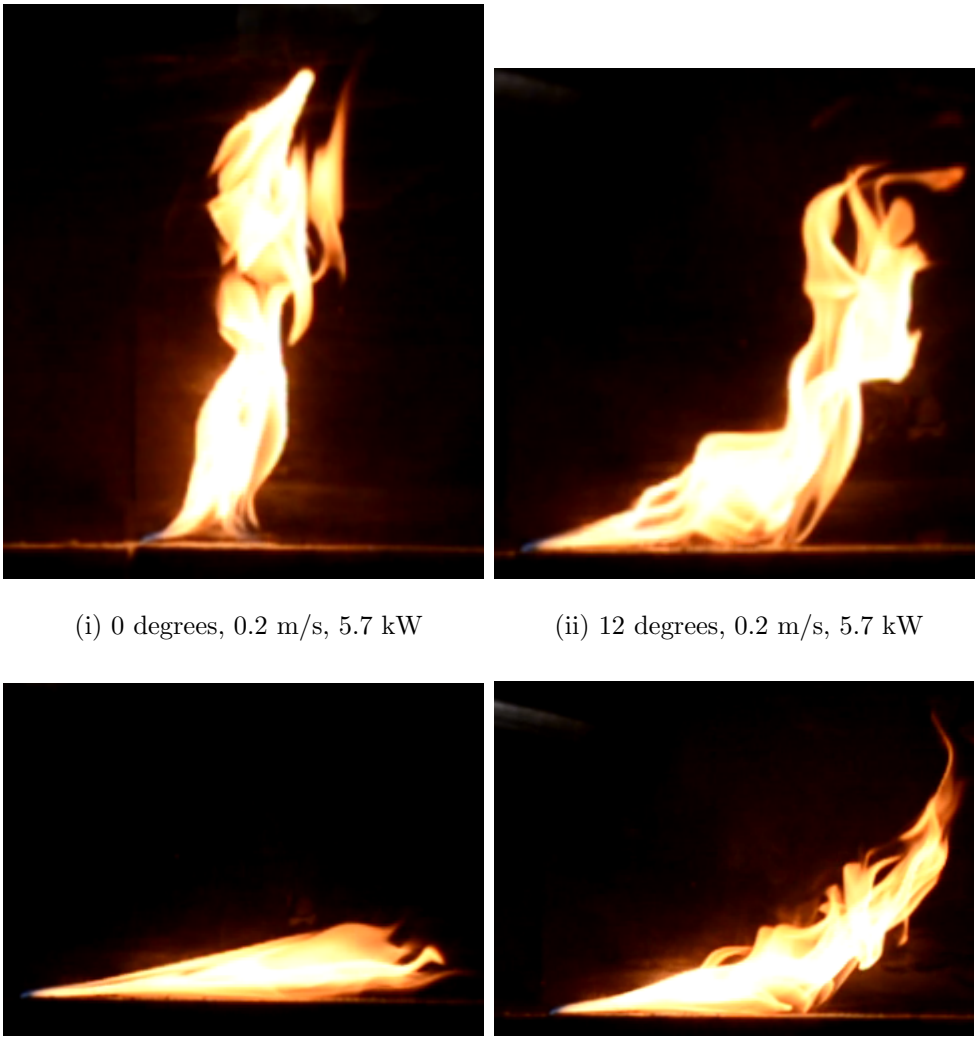

(i) 0 degrees, 0.2 m/s, 5.7 kW

(ii) 12 degrees, 0.2 m/s, 5.7 kW

(iii) 12 degrees, 0.5 m/s, 5.7 kW

(iv) 12 degrees, 0.5 m/s, 8.5 kW

Figure 4.1: Example images from the side-view video data collected under multiple conditions.

found in Table 3.1.

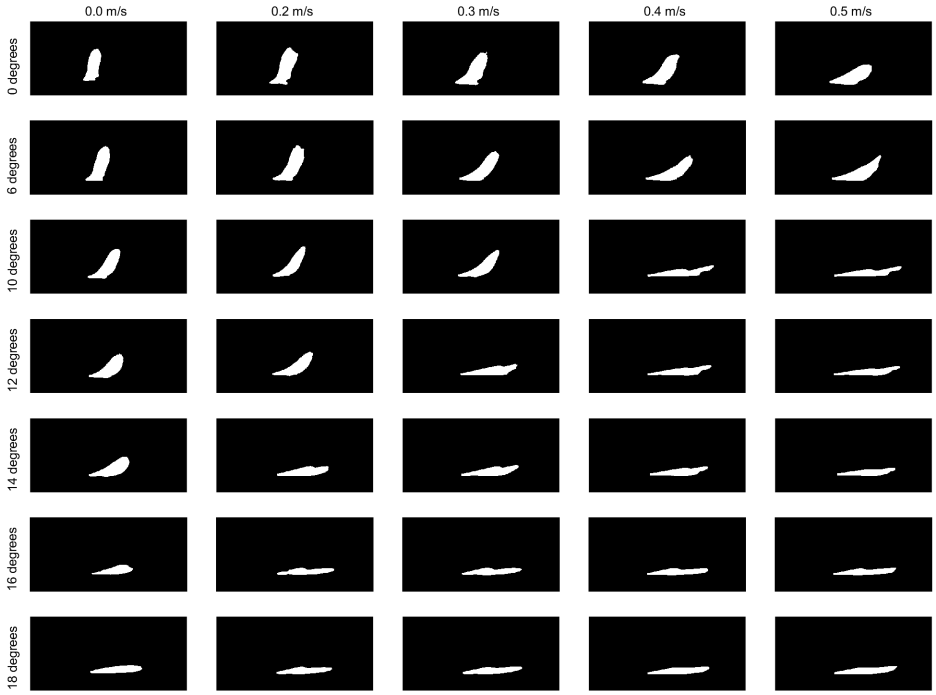

Figure 4.2: Flame image montage showing increasing tilt of the 2.8 kW flame as angle increases down the column of images, and wind increases across the row of images.

It is observed that at a certain combination of angle of incline and forced-flow wind speed, the flame moves from being buoyantly lifted from the surface, to being forced against the surface. Flame liftoff is indicative of the competition between buoyancy of the hot gases from the flame, and the momentum from the wind. The transition from buoyancy-dominated to momentum-dominated flames occurs almost diagonally across the frames in Fig. 4.2, showing that a combination of angle and wind contributes to the overall threshold for attachment.

4.2.1 Attachment Length

Flame attachment can be shown to vary with each independent variable. By isolating the variables, the singular effect of each can be observed. This is useful when trying to determine the combined effects that the variables have on attachment length. Attachment length is a relevant metric because it relates to the region ahead of the fire front that receives the most heating, increasing potential rates of flame spread.

The singular effect of wind can be assessed by analyzing the attachment length from tests where the angle of incline is equal to zero, and only the wind is changed. This is done for each HRR, as in Fig. 4.3. Forced-flow wind in this experimental setup does not have an overpowering effect on flame attachment. Without the increased effect from angle of incline, wind does not create total flame attachment on its own.

There is an increase in flame attachment in the intermediate wind speeds, however at the higher wind speeds, this effect is not as strong. This could be due to the wind not being able to overcome the buoyant forces from the flames.

The attachment length due to wind is dependent on HRR, a trend that will be observed in future sections. A correlation was not found for the attachment length due to wind alone.

The angle of incline of the experimental surface has a strong effect on flame attachment. Even without the increased effect from forced flow wind, inclination of the surface creates flame attachment on its own. The singular effect of incline can

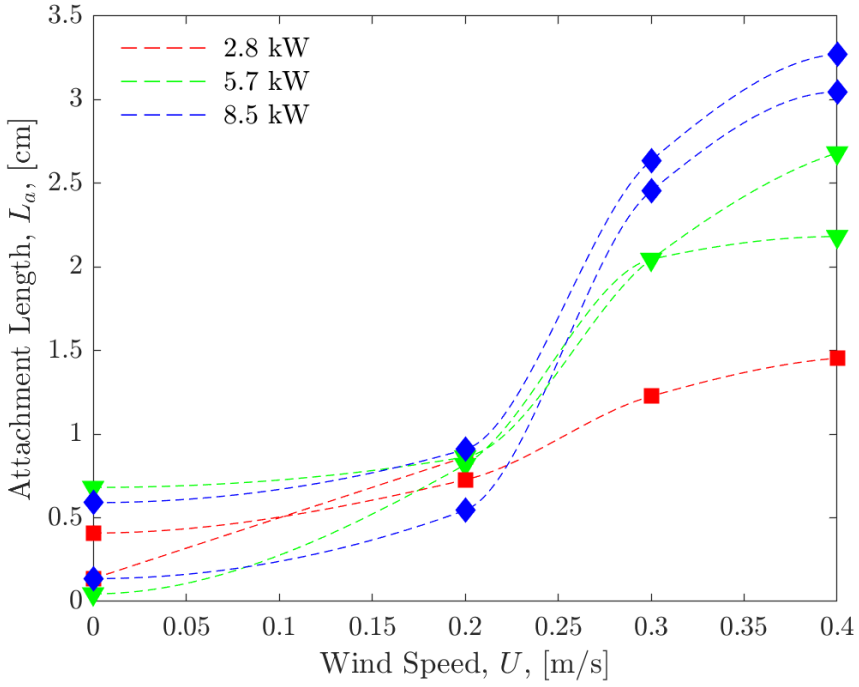

Figure 4.3: Increasing length of attachment as wind increases, for multiple HRR with no slope ($\theta = 0°$).

be assessed by analyzing the attachment length from tests where the wind speed is equal to zero, and only the angle of incline changes. This is shown in Fig. 4.4.

There appears to be a plateau for attachment length, where increasing the angle of incline does not increase the attachment length any further. From observation, this plateau appears when the flame fully attaches to the surface and the entire flame appears as a boundary layer. This makes the attachment length solely a function of HRR after a certain critical angle of incline for the cases without any applied wind.

The transition region from unattached to attached flames occurs mostly between 10 and 15 degrees for this experimental setup, making this the greatest area

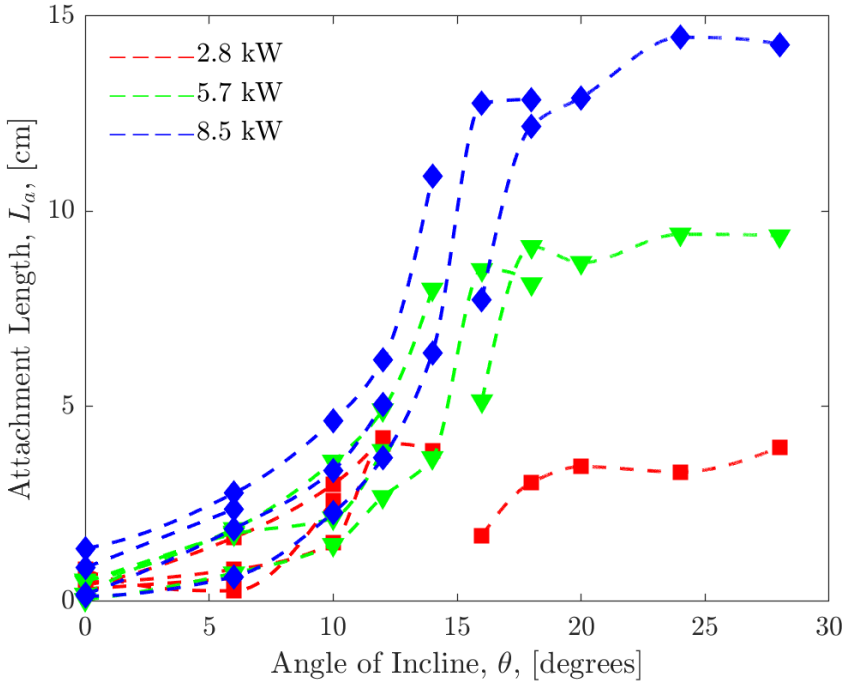

Figure 4.4: Increasing length of attachment as incline increases, for multiple HRR with no wind.

of focus for experimentation. After 18 degrees the flame is fully attached for nearly all cases with no wind applied. Applying wind will only increase the tendency to attach to the surface, meaning less inclination will be needed to achieve transition to a fully-attached flame.

This critical angle for flame attachment is comparable to previous experimental results found for flame spread experiments in an inclined trench [22, 49, 50], where the critical flame angle was found to be between 15° and 20°. The critical flame angle in experimental studies without sidewalls [5, 24, 50] was found to be between 24° and 28°. Some outliers in this trend exist; Smith [24] found a critical angle of 27° for an inclined trench of about the same dimensions as the experimental setup

in this study, but with fire sizes that are an order of magnitude larger than what was considered for this study. However, in general, the results from the current experiment match previous results, where the trench effect increases the propensity of flame attachment behavior, so that it occurs at lower inclination angles than studies with sidewalls removed.

The attachment length appears to be very dependent upon HRR after the flame attaches itself fully to the surface. To investigate this effect further, the length of attachment is shown in relation to HRR in Fig. 4.5.

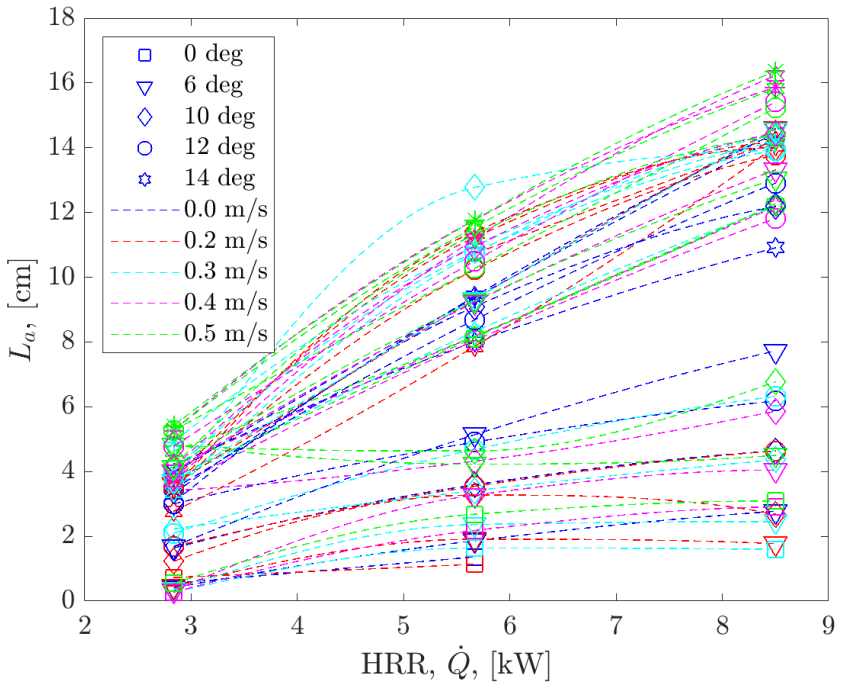

Figure 4.5: Increasing length of attachment, L_a, as heat release rate, HRR, increases for all wind speeds and angles of incline.

Though it is difficult to distinguish individual conditions in Fig. 4.5, it is clear that, overall, the attachment length increases with HRR. This appears to be true

whether or not the flame is fully attached in a boundary layer mode. There is a clear separation where some of the data points with a greater attachment length have a steeper slope. This represents the experiments where the flame was attached, and the attachment length solely depends on HRR, and not wind and slope.

To take a closer look at the relationship of attachment length to HRR, Fig. 4.6 shows a single wind speed, with multiple angles of incline.

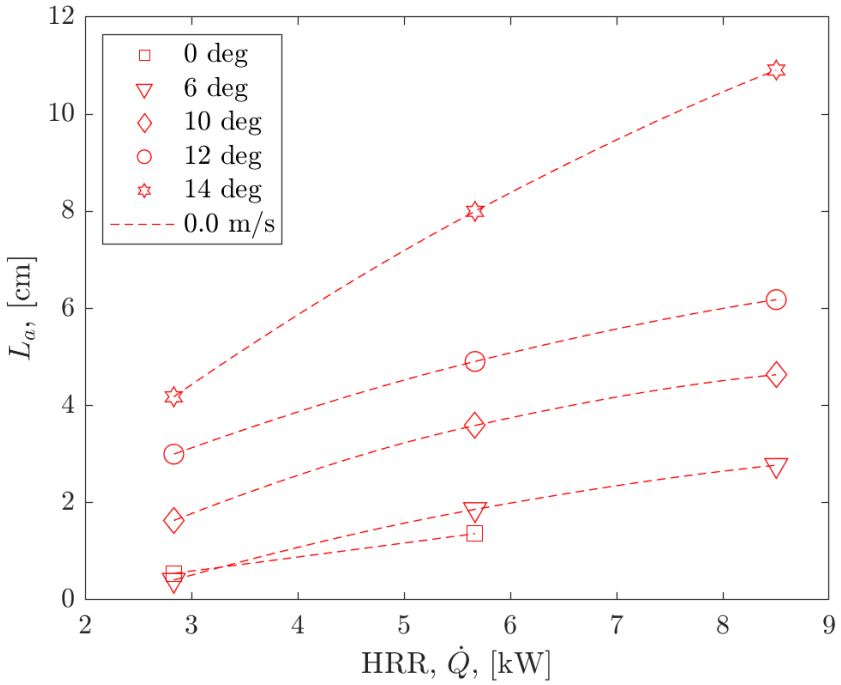

Figure 4.6: Increasing length of attachment as HRR increases, for no wind (0 m/s) and multiple angles of incline.

The same linearly-increasing trends are apparent in Fig. 4.6 as in Fig. 4.5. Only the 14 degree case with zero wind appears to be in the fully-attached regime with a steeper slope that indicates a stronger relationship between attachment length and HRR for the attached flames.

The flame length is defined here as the length of a straight line from the center of the burner to the flame tip, determined using the image-processing algorithm outlined in Sect. 3.4. It helps capture the overall fire size which relates to downstream heating. Fire size is therefore synonymous to HRR, and Fig. 4.7 shows how flame length is related to HRR.

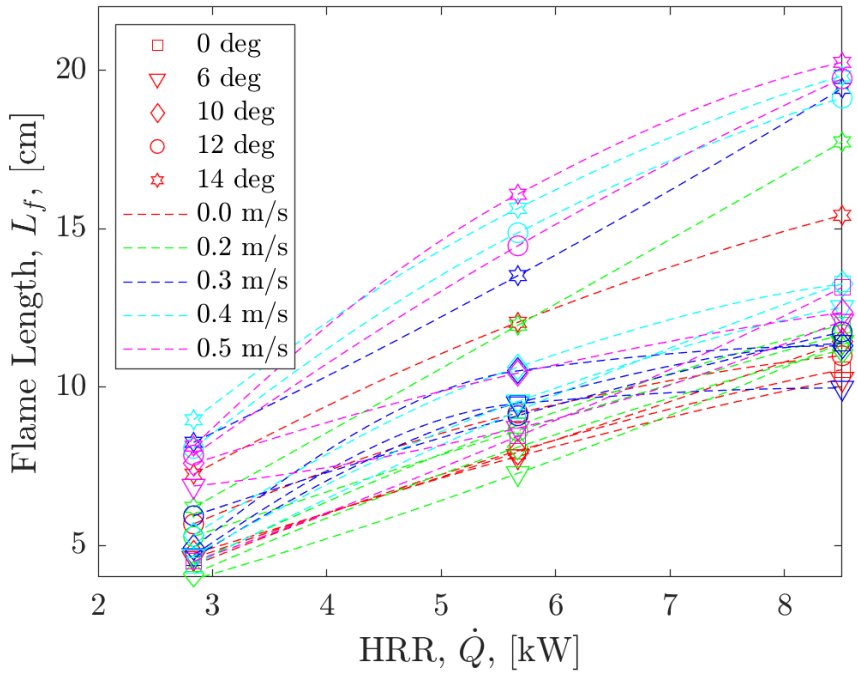

Figure 4.7: Increasing flame length as HRR increases, for all wind speeds and angles of incline.

The flame length also appears to have two regimes, attached and unattached, where the lines in Fig. 4.7 with the highest flame length also appear to have the steepest slope. Geometrically, the flame tip can extend further when the flame is fully attached as the flame is confined more to one dimension conforming to the straight-line definition applied here. There may also be other combined effects of

wind and slope to extend the flame further than if the two effects are competing.

To explore how the flame length effects downstream heating, it plotted as a function of the attachment length for all test conditions in Fig. 4.8

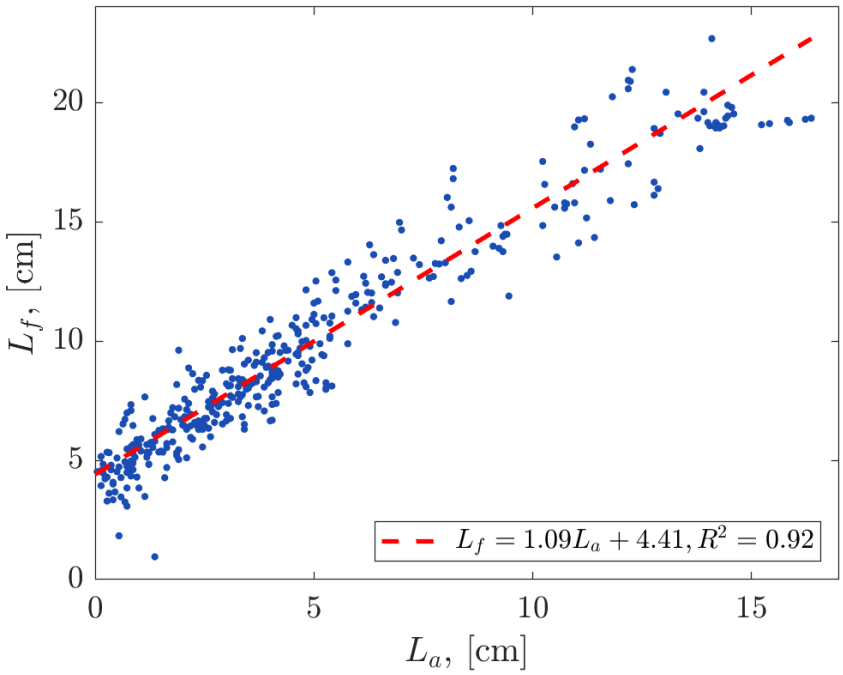

Figure 4.8: Increasing flame length as attachment length increases, for all data points.

The plot shown in Fig. 4.8 reveals a clear relationship between the flame length and attachment length, showing that applying inclination and wind lengthens the flame, proportional to increasing flame contact with the surface. This also shows that if either the flame length or the attachment length can be accurately predicted through other means, then the opposing value could also likely be predicted as the effect is essentially linear. The influence of external parameters were found to have little effect on this linear relationship of flame geometry, besides proportionally

increasing both values.

The flame angle with respect to the inclined surface is a useful metric to distinguish whether the flame is considered attached or not. The attachment length will intuitively be at its greatest with a low flame angle, because a low flame angle represents the tip of the flame being close to the surface. This is observed in Fig. 4.9.

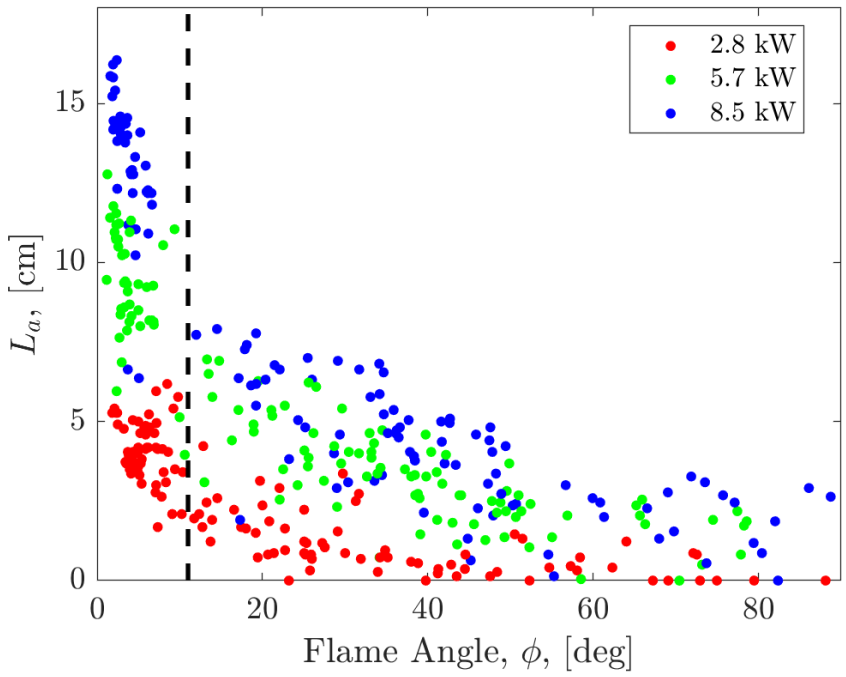

Figure 4.9: Decreasing attachment length as flame angle increases towards a vertical flame, grouped by HRR for all wind speeds and angles of incline. The dashed line represents the critical flame angle for attachment.

The dashed black line in Fig. 4.9 represents an approximate 12 degree critical flame angle, in which flame angles below 12 degrees describes an attached flame. This line is determined manually at the point in which the slope of the collective

data points of the individual HRRs appear to change drastically, as flame angle decreases.

The increase in attachment length as flame angle decreases is of course limited by HRR. In order to minimize the influence of HRR, the attachment length can be divided by HRR as in Fig. 4.10. At this point, the 12 degree critical angle still appears to well-describe this transition. Another flame angle was also noted here where the slope of the collective data points appears to change again. The attachment length does not begin to increase until flame angles below 55 degrees. This was determined as a transition flame angle from a fully buoyant flame to a flame exhibiting some forced flow behavior that begins to extend the attachment length.

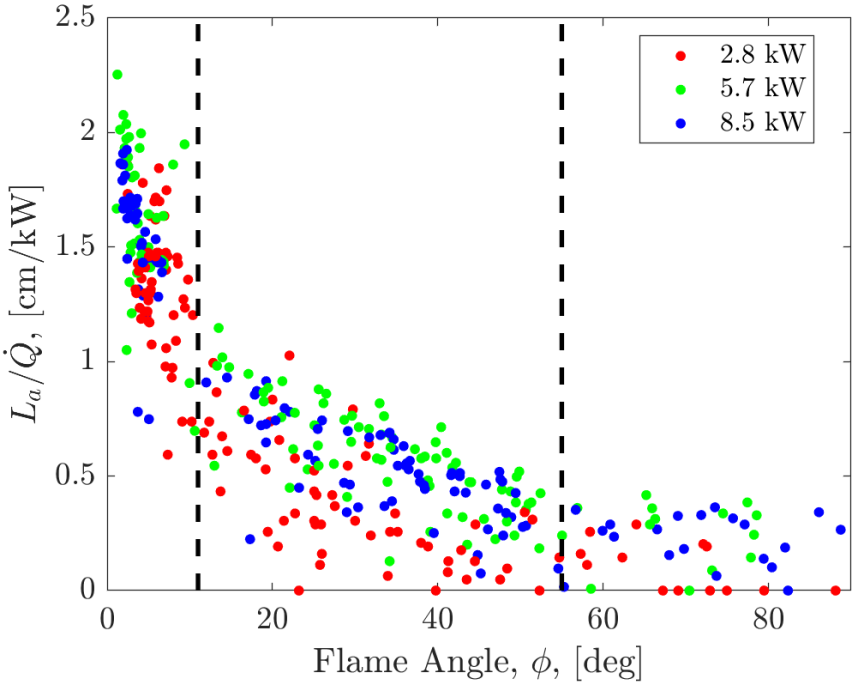

Figure 4.10: Decreasing attachment length as flame angle increases towards a vertical flame, grouped by HRR for all wind speeds and angles of incline.

The same graphical analysis in Fig. 4.9 and Fig. 4.10 can be applied to flame length. The plots look very similar as flame length and attachment length are linearly related, as determined from Fig. 4.8.

The flame height can also effectively be related to other measures of flame geometry. Fig. 4.11 uses increasing flame height to show increasing flame length in two regimes, attached and unattached. These regimes were determined by the 12 degree critical flame angle found in section 4.2.5.

The critical flame angle continues to well-describe transition to the attachment regime. By applying the 55 degree transition flame angle, Fig. 4.12 shows that there

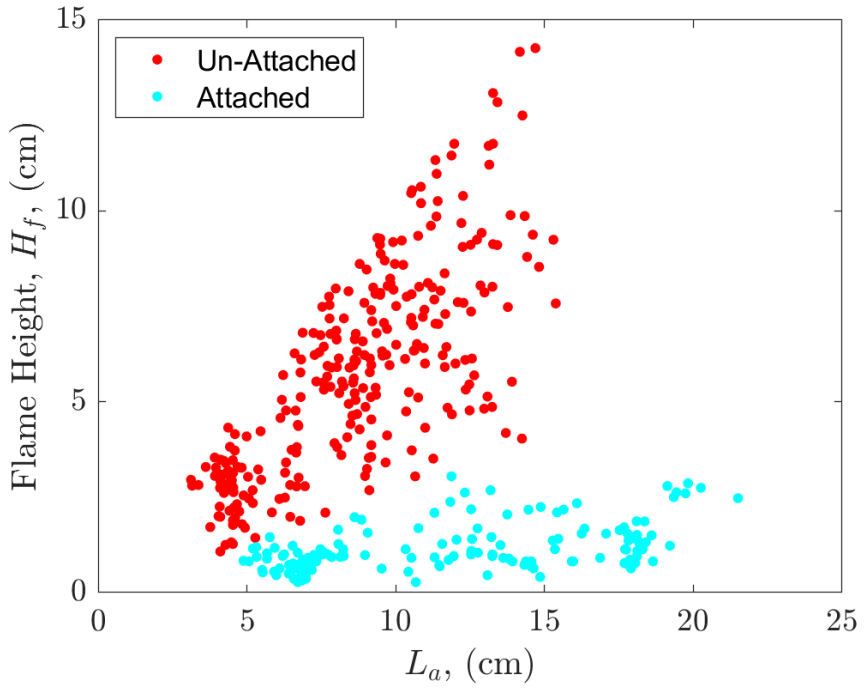

Figure 4.11: Increasing flame height as flame attachment increases, grouped attached and unattached regime determined by critical flame angle of 12 degrees.

can be three clearly-divided regimes in which the flame height can be related to the attachment length. The unattached regime is not particularly interesting because it is a simple gaseous burner with a buoyant plume. The attached regime is of interest, and it is known to be largely a function of HRR. The transition regime is probably the most important area of study. Determining when the flame will attach to the surface, and how much it attaches, is key in determining how much heat is applied to potential downstream fuels.

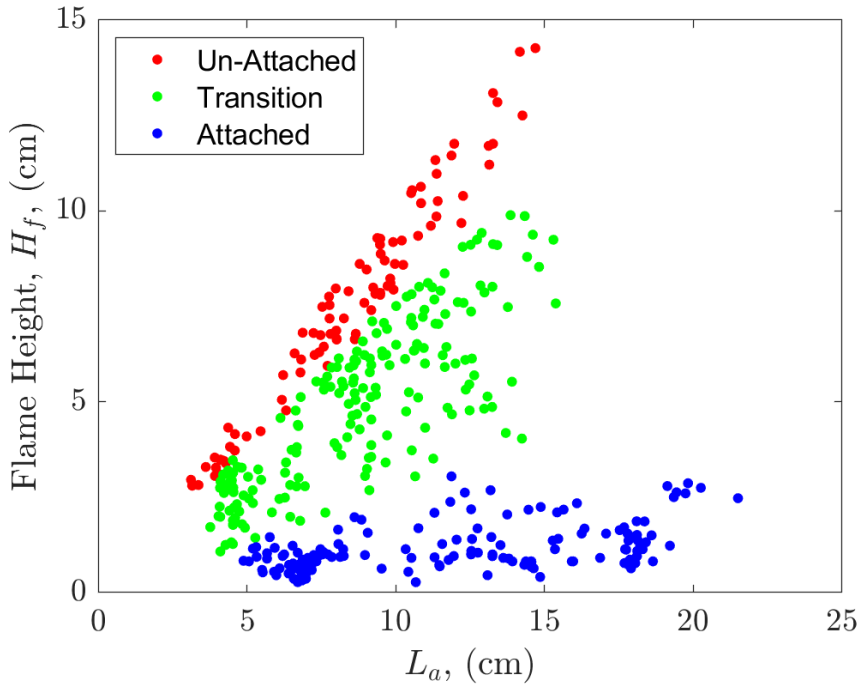

Figure 4.12: The flame height is shown based on the attachment length. The attached regime includes all flame angles below 12 degrees. The transition regime is between 12 degrees and 55 degrees. The unattached regime includes all flame angles above 55 degrees.

The critical flame angle and transition flame angle provide clear thresholds that allow for determination of whether the flame is attached without relying on subjective observations. Fig. 4.13 and Fig. 4.14 shows flames at each threshold of 12 and 55 degrees, respectively. The 12 degree flame angle is right on the cusp of where the flame will no longer exhibit any buoyancy-controlled characteristics and becomes fully attached to the surface. The 55 degree flame angle is the beginning of when the flame starts to attach to the surface and the attachment length begins to extend well beyond the burner. Identifying these points of transition allows for determination of basic characteristic of the flame's geometry, most notably attachment

which inherently describes the nature of downstream heating, directly affecting the flame spread rate.

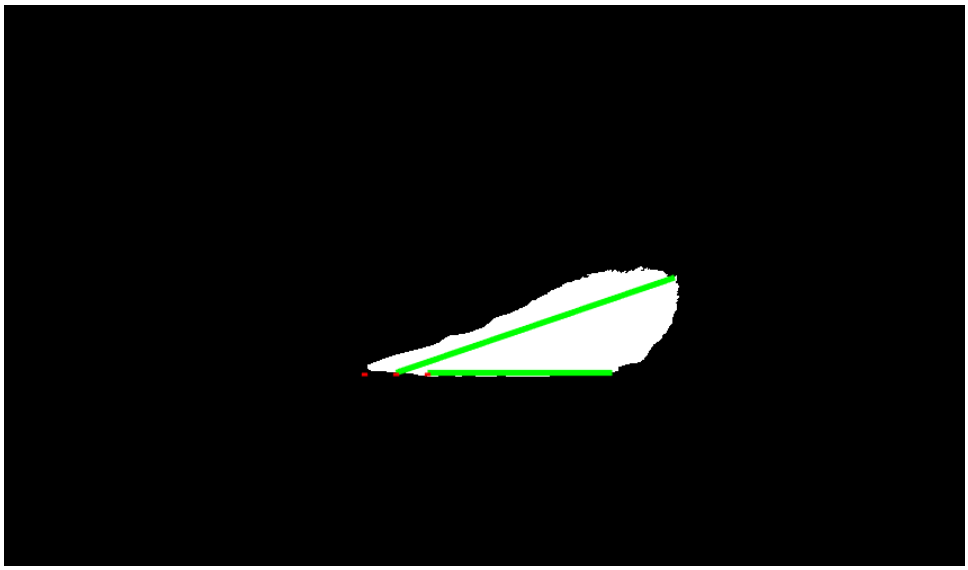

Figure 4.13: Image of a flame with an angle of 12 degrees from the horizontal surface. The line used to determine this angle is shown, projected from the center of the burner to the tip of the flame.

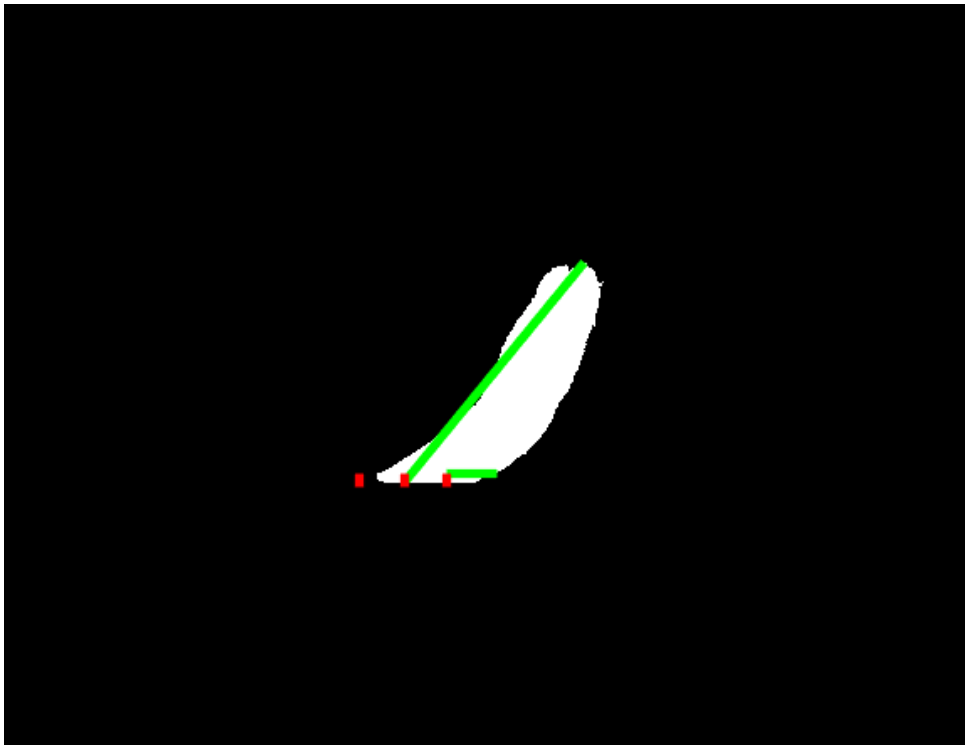

Figure 4.14: Image of a flame with an angle of 55 degrees from the horizontal surface. The flame is still mostly buoyant at this point, but the flame attachment is beginning to extend well beyond the burner.

4.3 Surface Heat Flux

Total heat fluxes measured using a water-cooled gauge on the surface downstream of the burner provides a measure of how much heat could be applied to downstream surface fuels during a spreading fire. This quantity is also related to the attachment length, as a higher heat flux is recorded at the surface when the flame is present. The raw heat flux data was found to fluctuate with time, as the flame is only truly "steady" when completely attached to the surface in a boundary-layer mode. For flames that are unattached or in transition, unsteady behavior is

observed consisting of buoyant turbulence. An example of this is shown in the raw data for a single test in Fig. 4.15. It is known that wildland fire flames exhibit certain quasi-periodic motions that are potentially predictable [44]. However, the simplest mode of analysis is to simply average the raw data at each position. This is applying an assumption that the flame is steady throughout the test. Averaging the raw heat flux readings creates a single data point at each position that a measurement is taken. This provides a profile of the heat being applied to the surface at distances away from the steady flame front. Exemplary profiles for a range of conditions are shown in Fig. 4.16. Each profile has a shaded region representative of the standard deviation of the raw data at each point. It is not a true measurement of error, but provides a visual representation of the variation involved when averaging heat flux measurements of an unsteady flame.

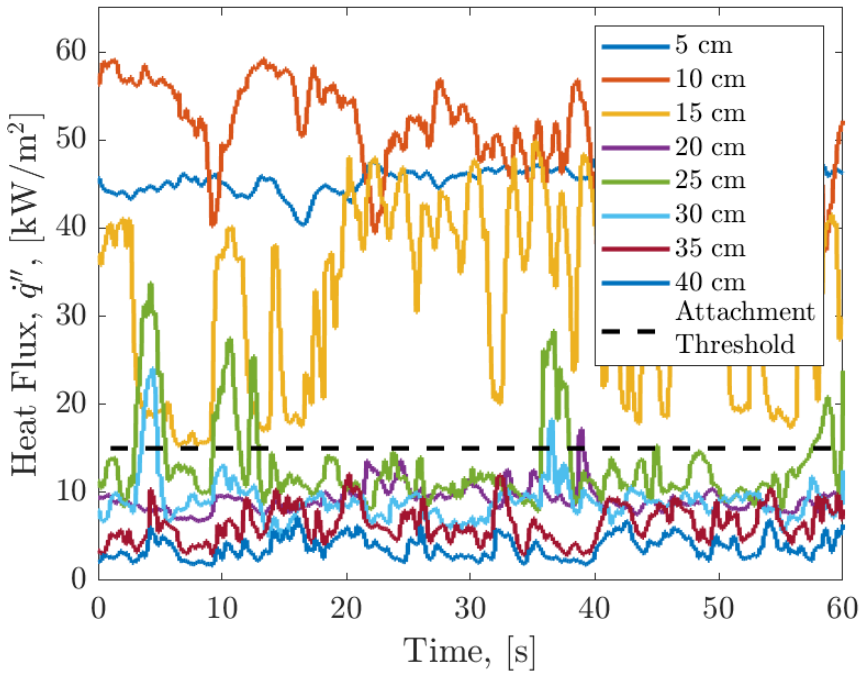

Figure 4.15: Example of raw heat flux data from a single test with 14 degrees of incline, 0.5 m/s of wind, and 8.5 kW HRR. The dashed line represents the threshold at 15 kW/m^2 that determines if the average heat flux reading shows that the flame is present at that gauge, indicating an attached flame.

In Fig. 4.16 the heat flux profiles have a steep decline to near zero at a certain distance past the burner. Before this decline the heat flux is much higher, and it can be assumed that the flame is present near the surface at the location of the heat flux gauge measurements. An arbitrary threshold value of 15 kW/m^2 determines if the flame is attached to the surface at each measurement location. The flame attachment distance determined using the furthest measurement of an average surface heat flux above the threshold value can be compared to the attachment length found using side-view images under the same external conditions as in Fig. 4.17.

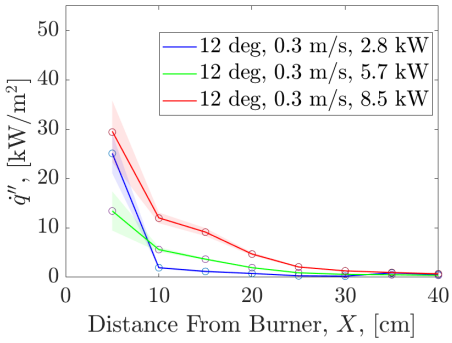

(i) 12 degrees, 0.3 m/s, varying HRR

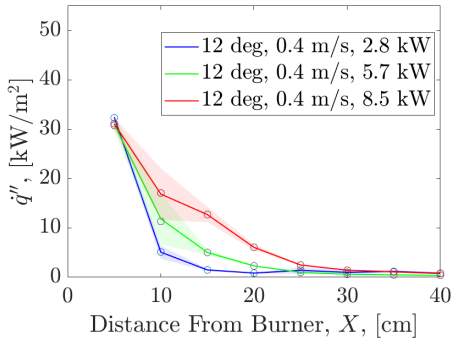

(ii) 12 degrees, 0.4 m/s, varying HRR

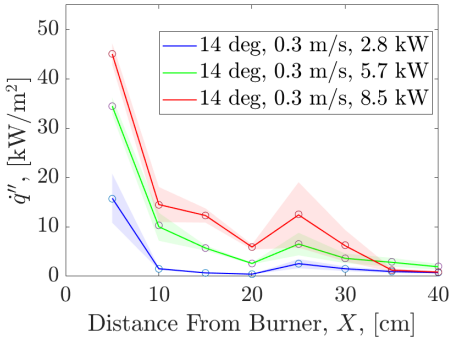

(iii) 14 degrees, 0.3 m/s, varying HRR

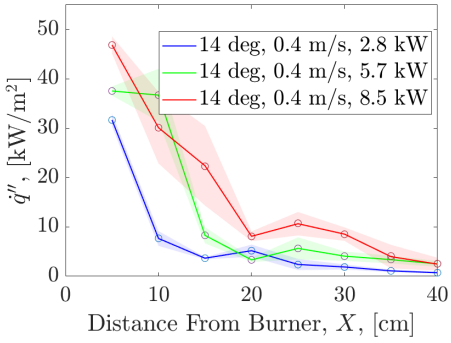

(iv) 14 degrees, 0.4 m/s, varying HRR

Figure 4.16: Example profiles of average heat flux data under varying test conditions. The shaded region associated with each profile represents one standard deviation from the average calculated from the time-dependent data.

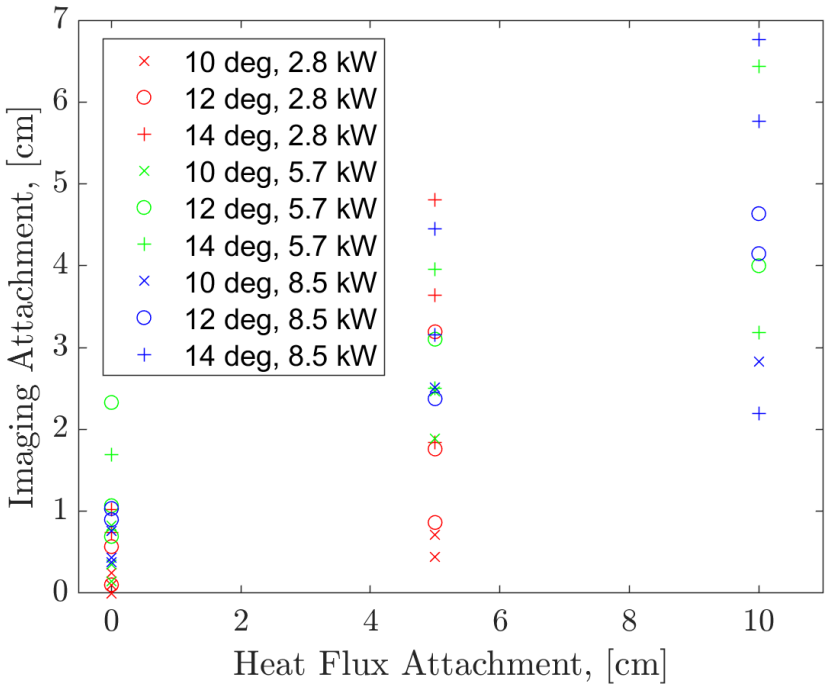

Figure 4.17: The heat flux attachment length compared to the attachment length found from side-view imaging measurements of the flame.

Markstein and de Ris [51] fit the heat flux applied to the surface ahead of a spreading flame front as a decaying power law function of downstream distance,

$$\dot{q}''(x) = A(x/x_p)^n, \tag{4.1}$$

where $\dot{q}''(x)$ is the surface heat flux as a function of the downstream distance, x, which is normalized by the pyrolysis length, x_p, which is the burner width for this stationary burner case. This equation was applied to each individual profile, and values for the constants A and n were fit to each profile. Fig. 4.18 is an example of such a profile with an associated fit. The values for n were found to be between -1 and -2.4. These values are smaller than what is found in Gollner et al. for spreading

and stationary PMMA flames, where the value for n was about -5 for angles of incline between about 0 and 30 degrees [13]. Note that the curve is only fitted to mean values, not accounting for the shaded region of the graph that is associated with the standard deviation of the raw data.

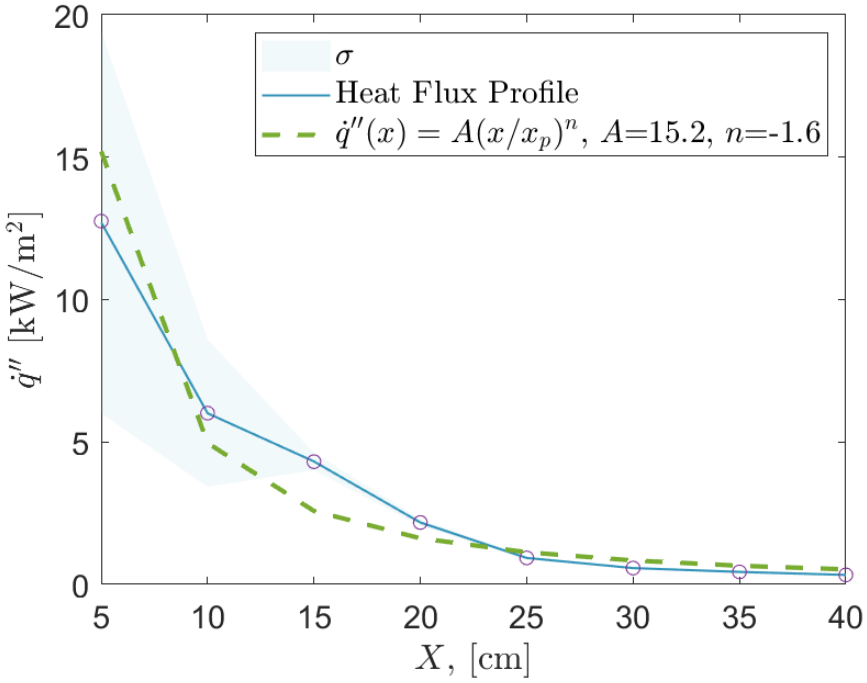

Figure 4.18: Example of a profile of average heat flux data from a single test condition, with the fit from Eqn. 4.1 applied.

The exponential decay fit parameters can be graphed as a function of the inclination angle, as in Fig. 4.19i and Fig. 4.19ii for coefficient A and exponent n, respectively.

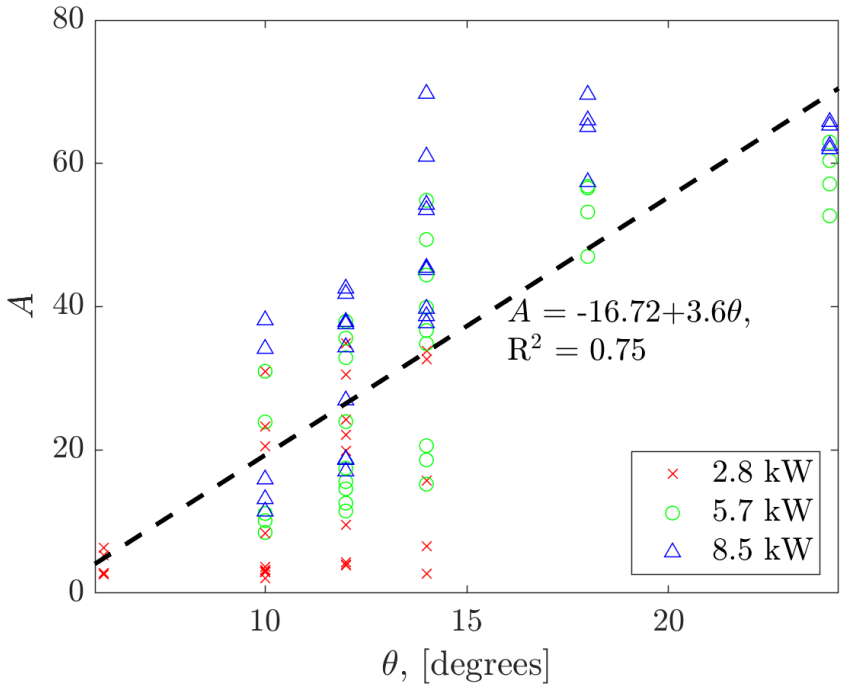

(i) Exponential decay fit coefficient, A.

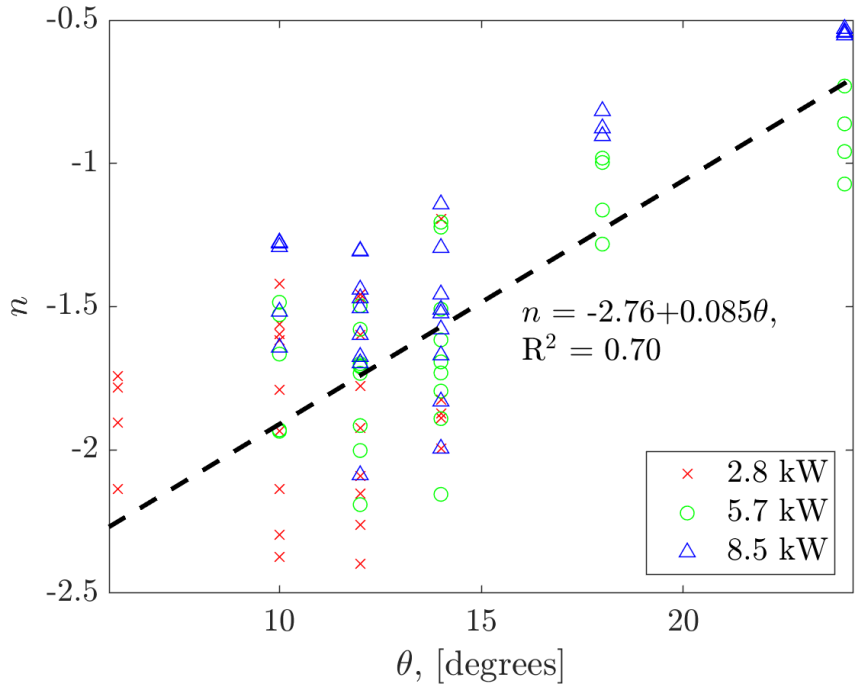

(ii) Exponential decay fit exponent, n.

Figure 4.19: Plots of the fit parameters for the exponential decay of the surface heat flux gauge.

4.4 Temperature Measurements

Temperature measurements were collected downstream of the burner as described in Section 3.3 in order to compare thermocouple measurement techniques to heat flux and imaging methods. The raw instantaneous temperature data was not temporally analyzed as thermocouple measurements are taken at only 2 positions at a time, and staggered 20 cm apart. However, the data was compensated for the thermal inertia of the thermocouple bead, and corrected for true gas temperature. The process used a dual-thermocouple probe method described in Sect. 3.6 outlined by [39] and developed by [42]. An exemplary plot of the compensated instantaneous temperature data for a single test condition is shown in Fig. 4.21. A comparison of the recorded measurements and the compensated gas temperatures is shown in Fig. 4.20i and their associated time constants 4.20ii. The calculated gas temperature clearly shows an instant, and much more extreme, temperature response compared to the two thermocouples, which have a slower response based on the size of the thermocouple bead. This can also be seen in 4.20ii, where the time constant is smaller for the smaller-diameter thermocouple, $\tau_{d,1}$.

However, the average temperature data taken over a 10-second time period reveals a temperature profile that shows the temperature perceived by the thermocouple at certain distances from the edge of the burner, shown in Fig. 4.22 for a single test condition.

The attachment threshold shown in Fig. 4.22 was as the point furthest from the burner that had an average value above 350°C. This value was chosen as it has

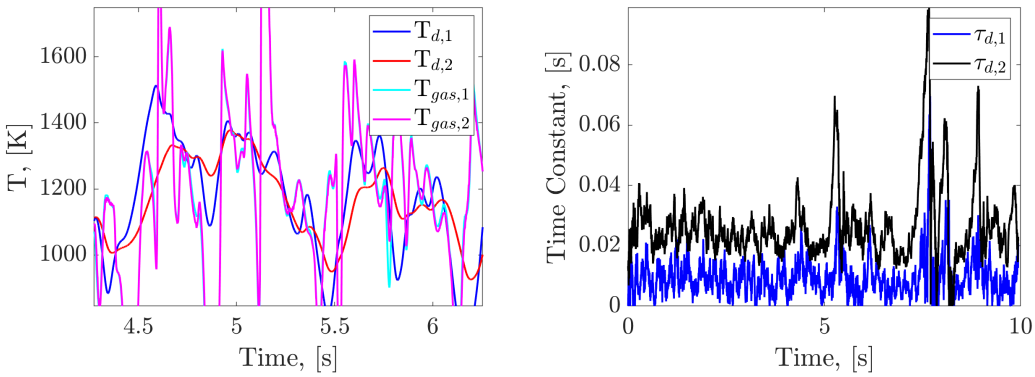

(i) (ii)

Figure 4.20: Comparison between the raw instantaneous temperature measurements (T_d) and the compensated gas temperatures (T_{gas}) is shown in 4.20i. The gas temperatures should be essentially identical, which is why it appears as one line. Time constants calculated are shown in 4.20ii for the thermocouples of wire diameter 25 μm ($\tau_{d,1}$) and 75 μm ($\tau_{d,2}$).

been used previously to determine flame contact with thermocouples [44], and is used regardless of HRR or other conditions. If the threshold were to be adjusted in any way it may be valid to choose a threshold based on HRR, as a hotter flame will allow less convective cooling from the wind-blown air, and higher temperatures will be measured. It is important to note that the temperature profile initially increases for many conditions, until peaking and decaying at a certain distance past the burner. The low temperature near the burner is due to the thermocouple being located 1 cm above the surface, about where the top of the forced-flow boundary layer is located. As the thermocouple traverses downstream, it moves through the

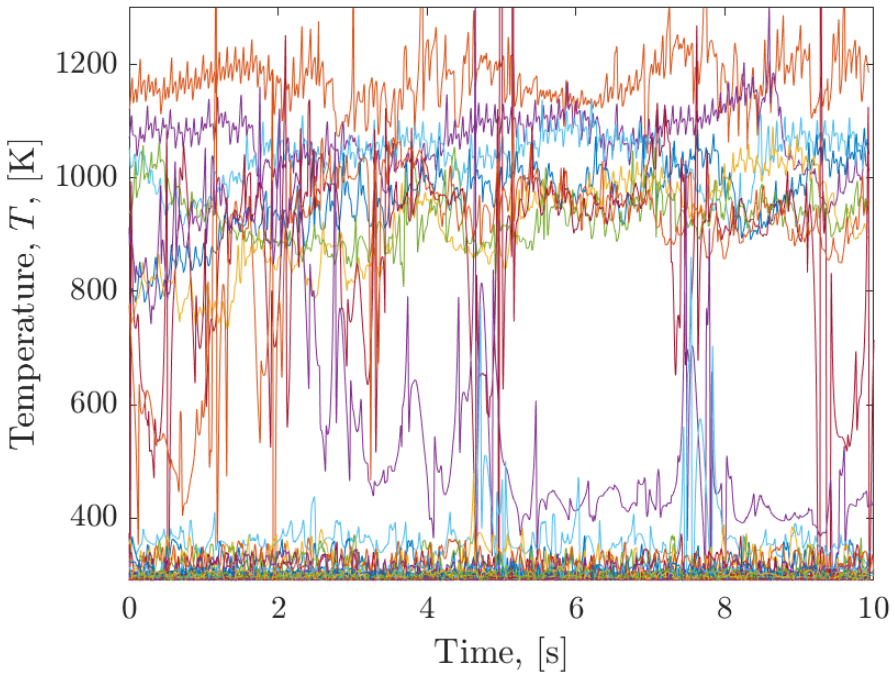

Figure 4.21: Example of the raw instantaneous thermocouple data, taken at 5 kHz, from a single test at 16 degrees of incline, 0.3 m/s wind speed, and 5.7 kW HRR. Each colored line in the plot represents a single compensated thermocouple measurement at a specific distance downstream of the burner. Temperatures are generally steadier for lower-temperature unattached or higher-temperature attached regions, with significant fluctuations observed at intermediary distances.

flame. At the plateau of the temperature profile the thermocouple is either fully immersed in the flame or is within the unsteady buoyant flame that occurs when the flame has "lifted-off" from the surface. These unsteady temperature readings near the plateau are due to the flame being unstable in this region, fluctuating between a lifted and attached state.

A lognormal distribution was fit to the temperature profiles downstream of the burner as it was determined to best represent the observed profiles. The choice

of an appropriate fit is difficult as the initial (pre-peak) increasing region is not always observed, however a lognormal fit still clearly displays broader trends observed between configurations. Profiles are presented in Fig. 4.23 as histograms of temperatures above ambient, then fit to a log-normal distribution. When considering only the positions at which the flame was determined to be present (>350°C) a lognormal fit with mean, μ, and standard deviation, σ, was applied to each temperature profile as in Fig. 4.23i and Fig. 4.23ii. The log-normal fit and histogram can then be scaled to the expected value of the temperature reading above ambient, shown in Fig. 4.23iii and 4.23iv.

The log-normal fits have unique μ and σ parameters for each set of external conditions, and the fits can be shown in a single figure for varying conditions, as in Fig. 4.24. It is very clear that, with more wind applied at a particular incline and HRR, the μ shifts further downstream of the burner and the σ stretches out to cover the wider area where the thermocouples are registering flame present near the downstream surface.

The mean of the log-normal fits also shows somewhat of a trend with the angle of incline, as in Fig. 4.25i. That plot can be normalized by the wind speed for a tighter grouping, as in Fig. 4.25ii. The standard deviation of the lognormal temperature distribution, σ, can also be graphed against the external parameters. Fig. 4.26 shows σ having a downward trend as wind increases, for a variety of angle and HRR conditions.

In the next chapter, this threshold and its comparison to the attachment determined from thresholds for other measurement techniques will be compared to

assess the validity of each technique.

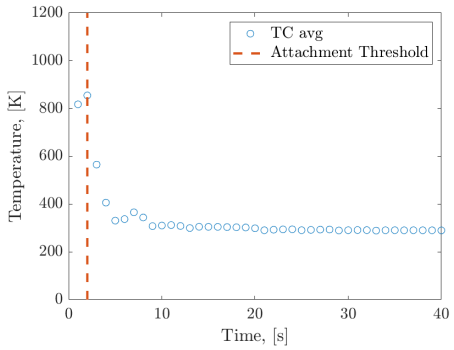

(i) 16 degrees, 0.0 m/s, 5.7 kW

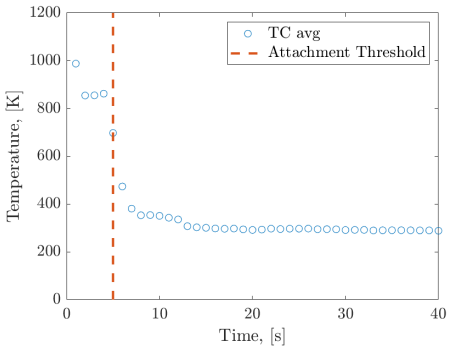

(ii) 16 degrees, 0.2 m/s, 5.7 kW

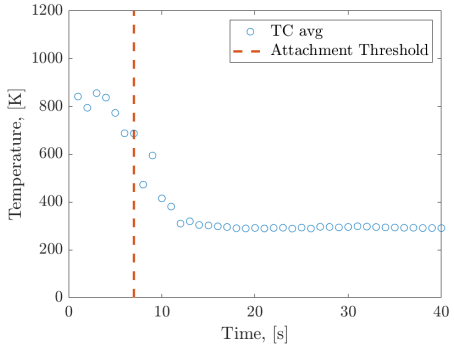

(iii) 20 degrees, 0.0 m/s, 5.7 kW

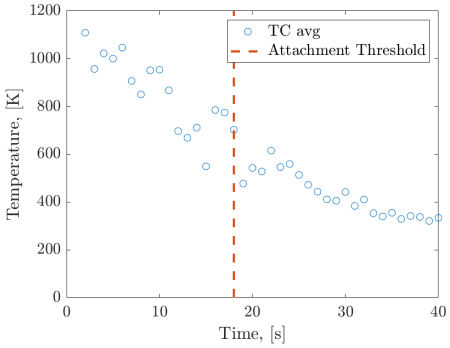

(iv) 20 degrees, 0.2 m/s, 5.7 kW

Figure 4.22: Example profiles of averaged thermocouple data from multiple test conditions. Each data point corresponds to an average of 10 seconds of thermocouple data taken at a specific distance, 0 cm to 40 cm, downstream of the burner. The vertical line represents the threshold of an average temperature of 350°C taken for the presence of flame attachment.

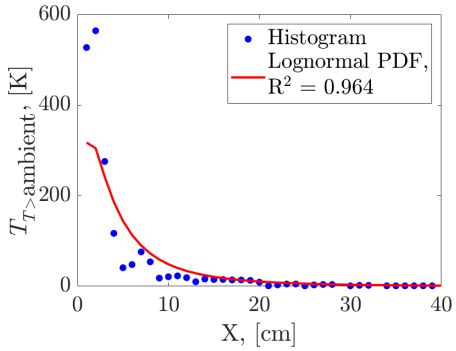

(i) 16 degrees, 0.0 m/s, 5.7 kW

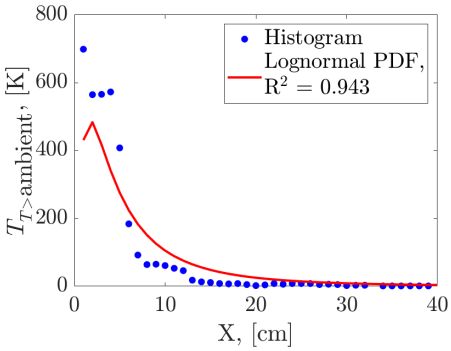

(ii) 16 degrees, 0.2 m/s, 5.7 kW

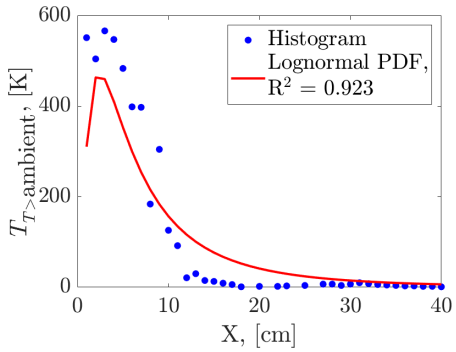

(iii) 20 degrees, 0.0 m/s, 5.7 kW

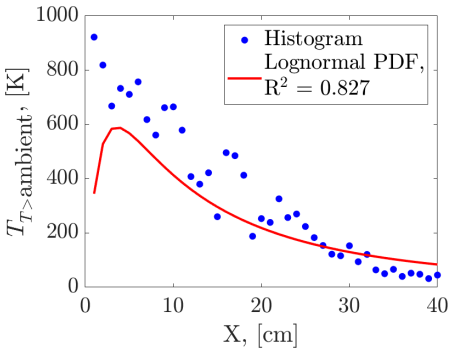

(iv) 20 degrees, 0.2 m/s, 5.7 kW

Figure 4.23: Example log-normal fit of temperature measurements across a range of conditions.

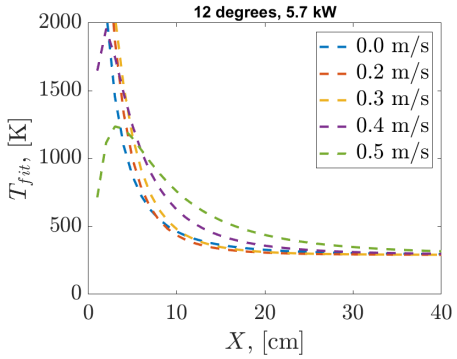

(i) 12 degrees, 5.7 kW. varying wind.

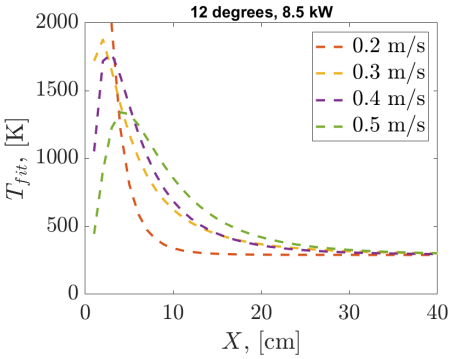

(ii) 12 degrees, 8.5 kW. varying wind.

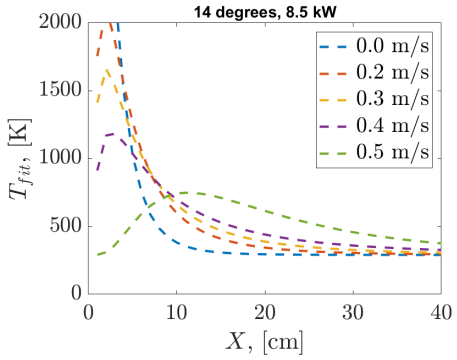

(iii) 14 degrees, 8.5 kW. varying wind.

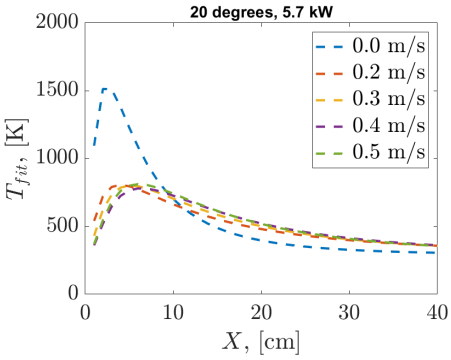

(iv) 20 degrees, 5.7 kW. varying wind.

Figure 4.24: Log-normal fits of the temperature profiles for varying conditions.

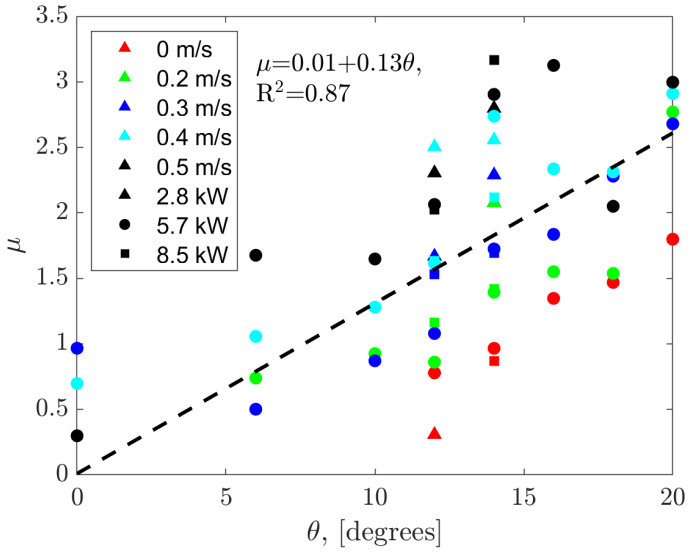

(i) 12 degrees, 5.7 kW. varying wind.

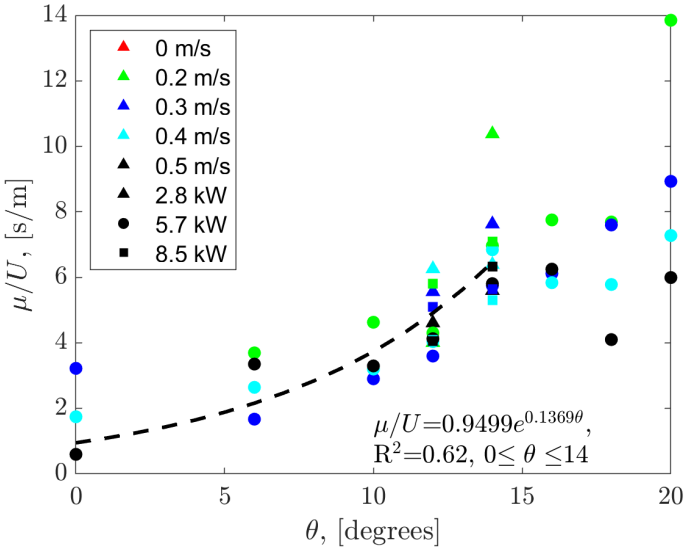

(ii) 12 degrees, 8.5 kW. varying wind.

Figure 4.25: Log-normal fit parameters, varied with inclination. In 4.25i, parameter μ from the log-normal fits of the temperature measurement profiles have somewhat of an increasing trend as a function of θ, the trend is stronger when μ is normalized by U in 4.25ii.

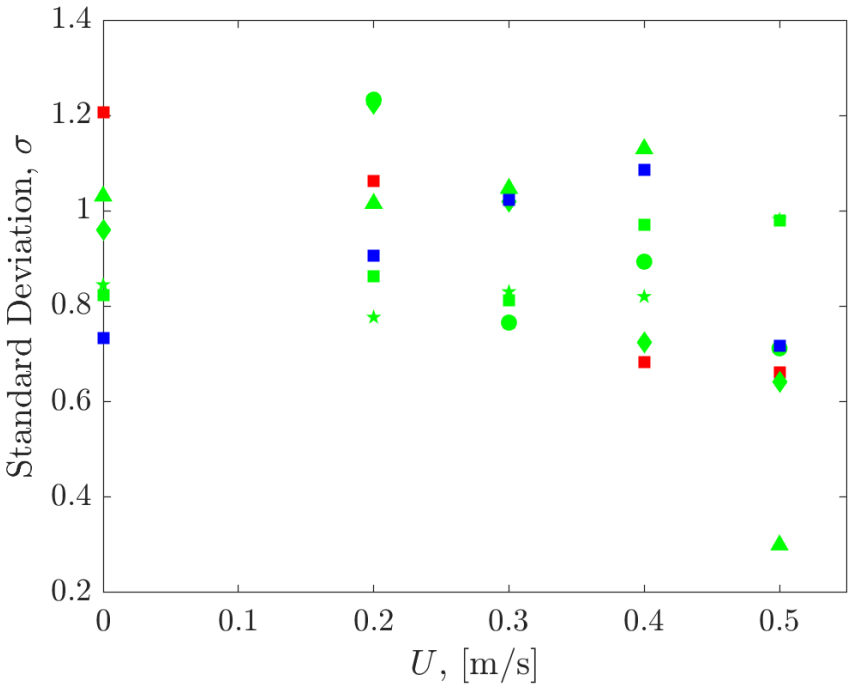

Figure 4.26: The standard deviation of the lognormal temperature distribution with a decreasing trend as wind increases. The colors represent separate HRR conditions, and the symbols represent different symbols, not necessarily revealing a trend.

Chapter 5: Discussion and Analysis

5.1 Overview

This chapter will provide in-depth analysis of the quantitative results from experimentation that were conveyed in chapter 4. The measurements of the flame structure taken from side-view imaging will be correlated by reducing the data to established non-dimensional numbers. The measured flame attachment from imaging will also be compared to the heating profiles and attachment thresholds discussed for both surface heat flux and fine-wire thermocouples. The presentation of these analyses will be followed by further discussion describing what the data comparison reveals about the ability of the measurement techniques to measure the phenomenon affecting spreading wildland fires.

5.2 Combined Effects On Geometry

As determined in the previous chapter, if any one parameter of flame geometry can be predicted, it would also be possible to predict the rest of the flame geometry. The attempted prediction of flame geometry through a combination of multiple individual variables will be shown.

The independent variables of wind, slope, and HRR have somewhat predictable singular effects on the flame behavior with respect to it's geometry and attachment to the surface. All of the flame's geometry, including attachment, appear to be very closely related. However, to make accurate predictions of how a flame will behave under any circumstances, these independent variables must be combined. Ideally, a function would emerge that is normalized with no units so that it could be easily scaled and applied to any experimental setup. This was first attempted by applying simple combinations of independent variables to varying degrees by applying powers to increase or decrease their influence. The purpose is to discover if there are trends in the flame geometry that are a function of the input parameters.

By simply multiplying all of the independent variables and comparing that to attachment length, Fig. 5.1 shows the relationship between the attachment length and all of the independent variables, grouped using the critical attachment and critical transition flame angles. There is a very tight grouping in this plot for the unattached and transition regimes. The attached regime somewhat mixes into the unattached regime, and is much more spread out. However, both appear that they could be correlated in a logarithmic or linear relationship.

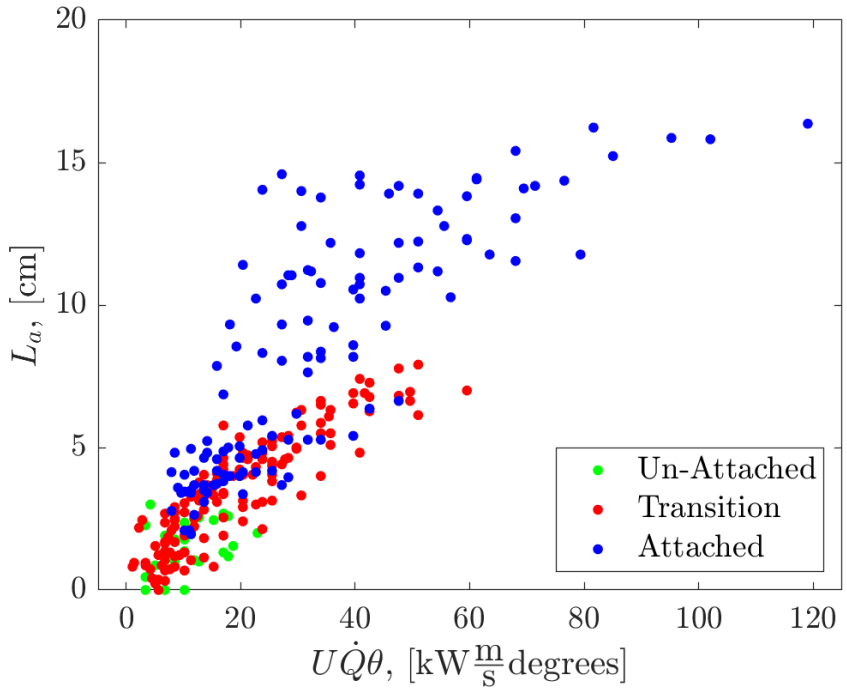

Figure 5.1: Increasing attachment length against a combination of the independent variables, grouped by the attached, transition, and unattached regimes determined by the transition and critical flame angles of 55 and 12 degrees, respectively.

The group of data points labeled as "Transition" in Fig. 5.1 were considered individually for a linear relationship in Fig. 5.2 that was found as,

$$L_a = 0.6802 + 0.14\,(UQ\theta)\,, \tag{5.1}$$

where L_a is in cm, and the units of $UQ\theta$ are [m/s kW degrees].

Neither of these plots provide a perfect correlation for predicting the downstream flame attachment length. However, they do show that there is, at the least, somewhat of a trend in the data. Furthermore, the trend depends on whether or not the flame is attached to the surface, based on a critical flame angle of 12 degrees.

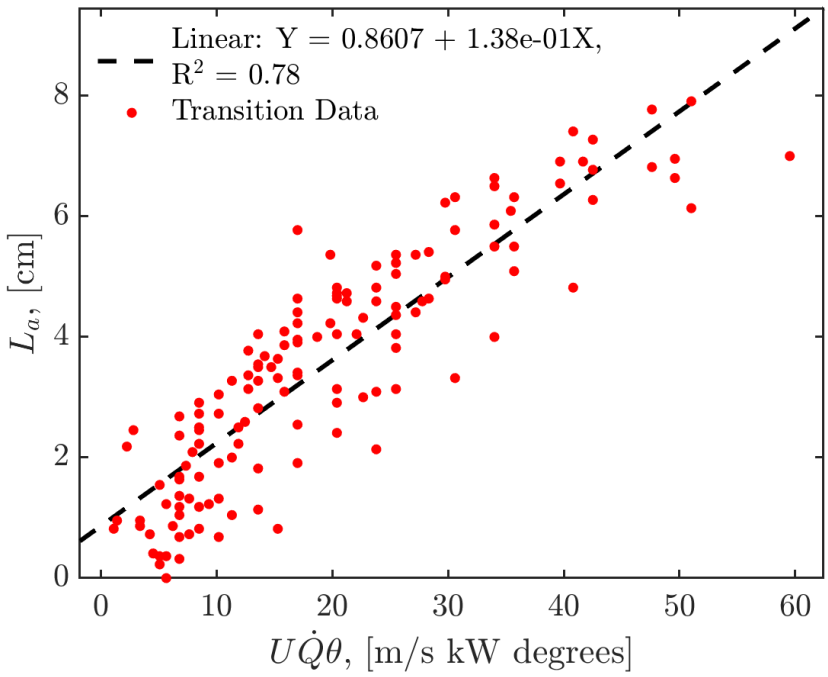

Figure 5.2: Increasing attachment length for transition data points against a combination of the independent variables for only the transition regime.

Predicting the flame angle allows for determining if the flame is attached to the surface, and possibly the actual flame attachment distance. Fig. 5.3 provides an arbitrarily found relationship between the flame angle and a simple combination of all of the independent variables.

It is clear that trends begin to appear between the flame structure and the independent variables of the experiment. To exploit these trends, non-dimensional numbers pertaining to fires that were previously derived from governing equations by Quintiere are utilized to explore trends that could apply to experiments at different scales [7]. The first of these variables, Q^*, represents the HRR as a non-dimensional

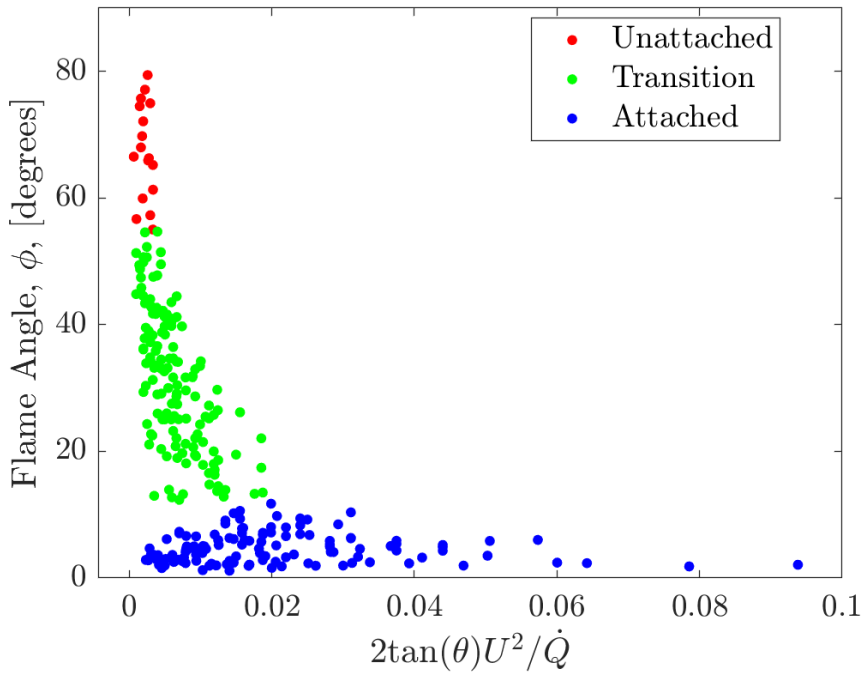

Figure 5.3: Predicting the angle of the flame using a combination of all independent variables. The colored groups provide a linear relationship at each wind speed, and the symbols provide the angle of inclination.

number

$$Q^* = \frac{\dot{Q}}{\rho_\infty c_p T_\infty \sqrt{g} L^{5/2}} \tag{5.2}$$

where $\dot{Q}$ is the HRR, ρ_∞ is density of air, c_p is the specific heat of air, and T_∞ is ambient air temperature, g is the acceleration due to gravity, and L is a characteristic length scale. This length scale L can be represented by either the flame length, L_f, or the burner width, L_w. From the equation for Q^*, the characteristic length can be represented as

$$L^* = \left(\frac{\dot{Q}}{\rho_\infty c_p T_\infty \sqrt{g}} \right)^{2/5} \tag{5.3}$$

where L^* represents a characteristic buoyant length scale with units of m. This can be used to non-dimensionalize other length scales describing the flame structure. A similar equation for a characteristic buoyant velocity, U^*, can be shown as

$$U^* = \sqrt{gL} \tag{5.4}$$

where U^* has units of m/s and can be used to normalize the ambient air velocity [7]. The Froude number, Fr, represents the competition of forced flow and buoyancy through the normalization of velocity as

$$Fr = U/\sqrt{gL}. \tag{5.5}$$

The simple relationship in Fig. 5.1 can be made non-dimensional, shown in Fig. 5.4. L_a is normalized by the length scale of the fuel source, L_w. $\dot{Q}$ and U are represented as non-dimensional Q^* and Fr, respectively. The inclination is represented as a $\sin(\theta)$. Fits are applied to both the transition and attached regimes in this case, with similar results for the transition regime as in Fig. 5.2. It should be noted however, that the length scale L_w is the same for all tests, therefore the normalized plot is nearly identical to the plot with units. There is essentially a lack of a proper length scale that does not involve the flame geometry, since the burner is a controlled variable for all the experiments. If a flame geometry were to be used as a length scale, it would then not be a predictive function, as a measurement of

the flame would be needed as an input. If the flame length is used as a length scale in the non-dimensional numbers, as in Fig. 5.5 results are more of a function of the flame geometry, and the linear-fit functions are not predictive, since you would need a measurement of the flame geometry as an input. The function is fit to a logarithmic scale in the x-axis in Fig. 5.6, with an R^2 of 0.75. It should be noted that a typical way to non-dimensionalize the attachment length is through use of L^* in Eqn. 5.3. However, this makes the normalized attachment length a function of $\dot{Q}$, which interferes with the x-axis input, which is also a function of $\dot{Q}$.

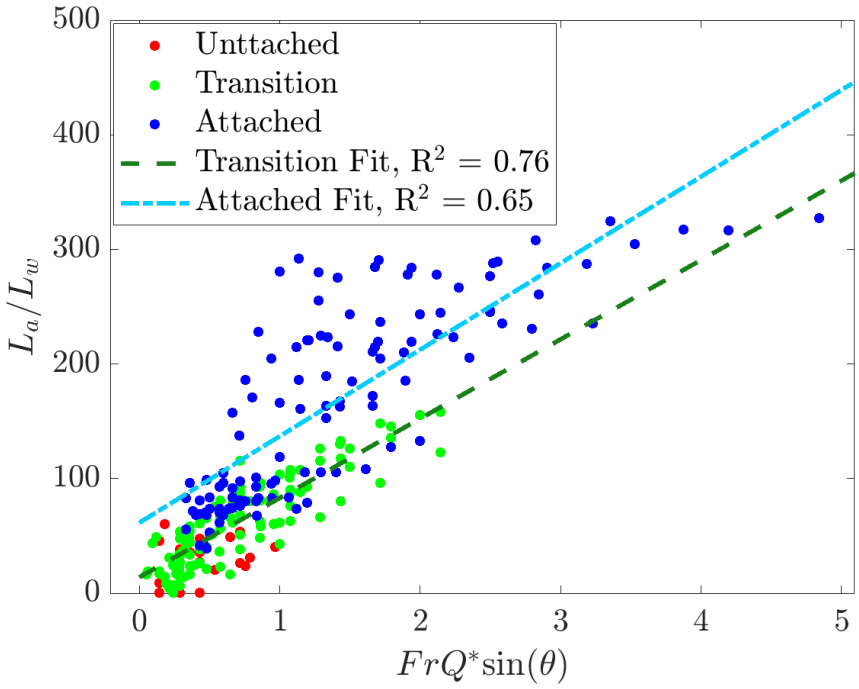

Figure 5.4: The attachment length normalized by the burner width is shown as a function of the non-dimensional numbers. The burner width, L_W, is the characteristic length, l, in the non-dimensional relationships.

All of the non-dimensional numbers can be manipulated to include a value for

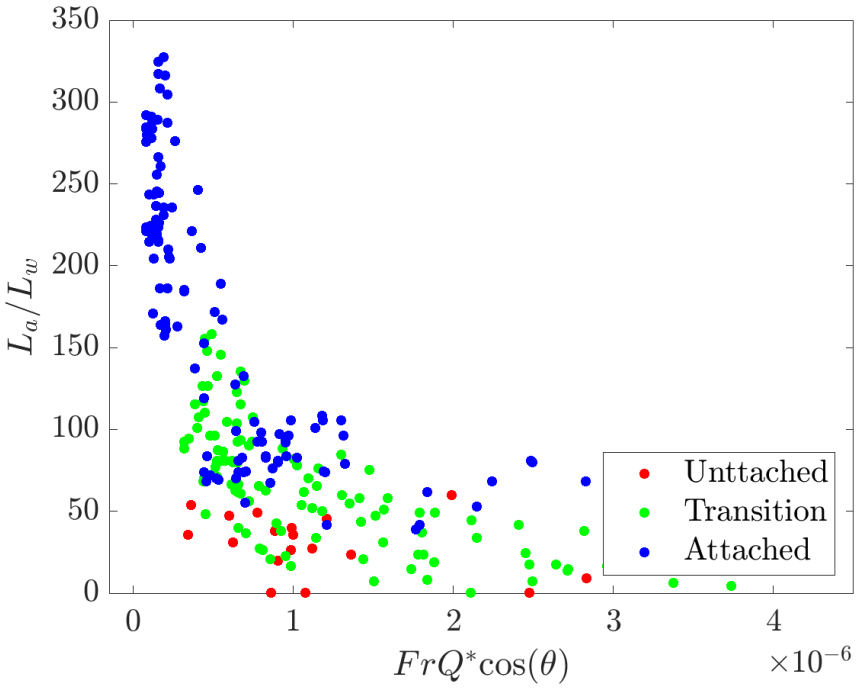

Figure 5.5: Depicting the length of attachment normalized by the burner width, as a function of Q^*, Fr, and $\sin(\theta)$. The flame length, L_f, is the characteristic length in the non-dimensional relationships.

the angle of inclination. By incorporating the angle into the term for the acceleration due to gravity $\sqrt{g\sin(\theta)}$, the consideration of gravity will no longer be vertical, but will be perpendicular to the slope of the surface, and therefore the direction of the forced flow. The numbers that include this term for angle of incline will be considered as Q^*_θ, L^*_θ, and U^*_θ.

Using the non-dimensional Q^*_θ and normalized attachment length, L_a/L^*_θ, with the $\sqrt{g\sin(\theta)}$ and using L_f as the characteristic length, the normalized attachment length is shown in Fig. 5.7. A linear relationship with an R^2 of 0.89 was found for a normalized attachment length as

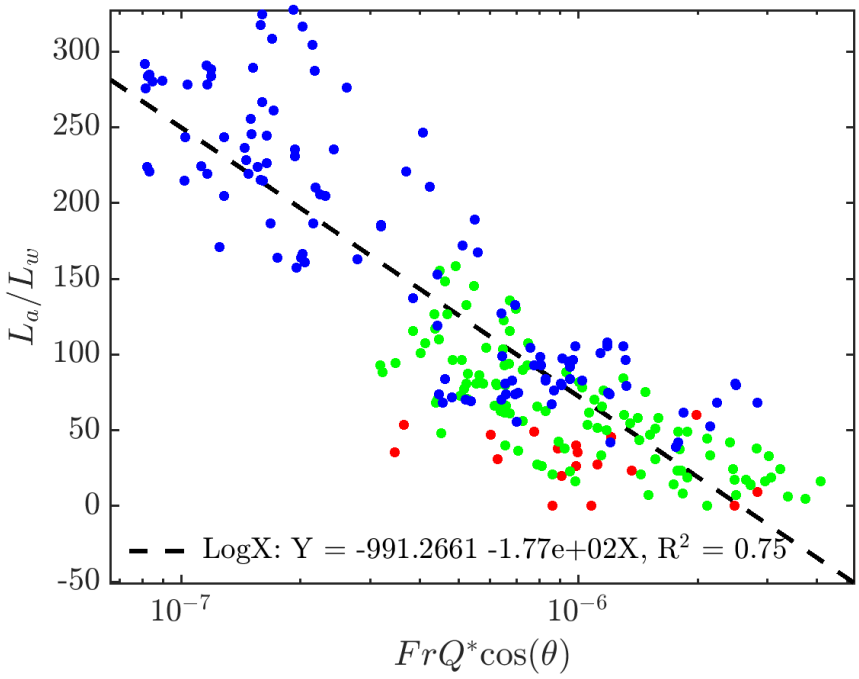

Figure 5.6: A negative linear relationship associated with the function in Fig. 5.5 is shown with a logarithmic x-axis.

$$L_a/L_\theta^* = -0.15 + 5.9 \times 10^{-5} Q^*. \tag{5.6}$$

It should be noted that both the Q_θ^*, L_θ^* contain the HRR, $\dot{Q}$, and the flame length, L_f. Therefore the HRR and flame length are represented in both the x- and y-axes. Although the representation of these values on both axes could potentially create a linear relationship in and of itself, these forces do not compete if you consider dividing the y-axis by the x-axis, as if you were determining the slope of the line. The creation of such a strong trend in this case is actually due more to the fact that L_f and L_a are very nearly linearly correlated, as shown in Fig. 4.8. This means that the relationship found in Eqn. 5.6 is not predictive. Though it does reduce the

parameters of incline and HRR to an effective linear relationship for understanding how flame length and attachment length are related. This could be useful knowledge, as further experimentation at different scales would be able to know what non-dimensional geometry their flame may take under different conditions. It is also possible that if a flame length is able to be qualitatively estimated, that would provide a known attachment length, which potentially predicts a fire spread rate.

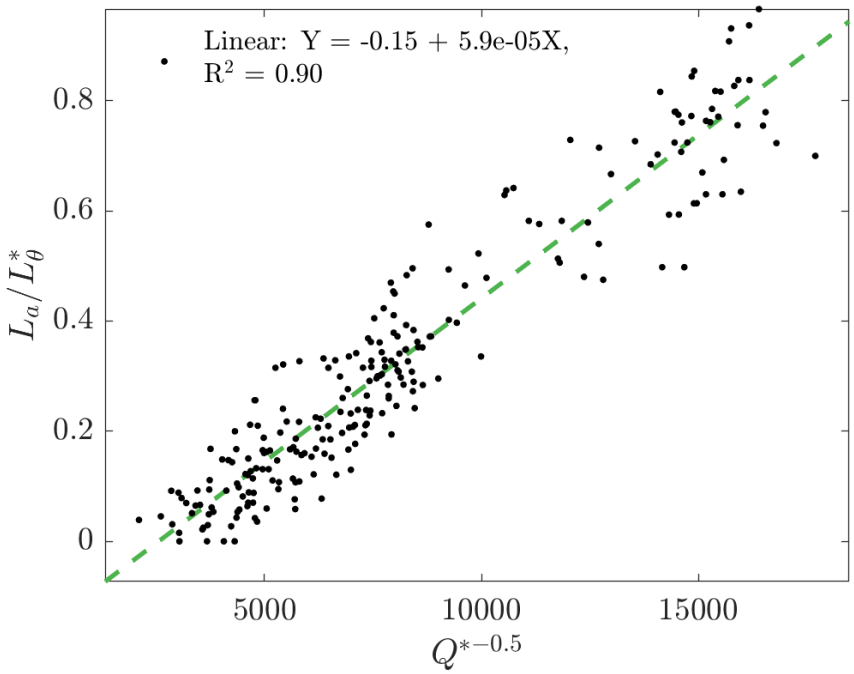

Figure 5.7: Normalized attachment length against a non-dimensional HRR, with the flame length as the characteristic length.

The attachment length, L_a, can also be non-dimensionalized by L^* in Fig. 5.8, normalized by the HRR using Q^*, and graphed against a combination of Q^* and the normalized velocity, U/U^*. There are 3 regions of interest that collapse into a measure of the attachment length, normalized by the heat release rate, based

on input of heat release rate and wind. If this relationship were explored further, it could potentially reveal non-dimensional relationships for the attachment length based on simple input parameters.

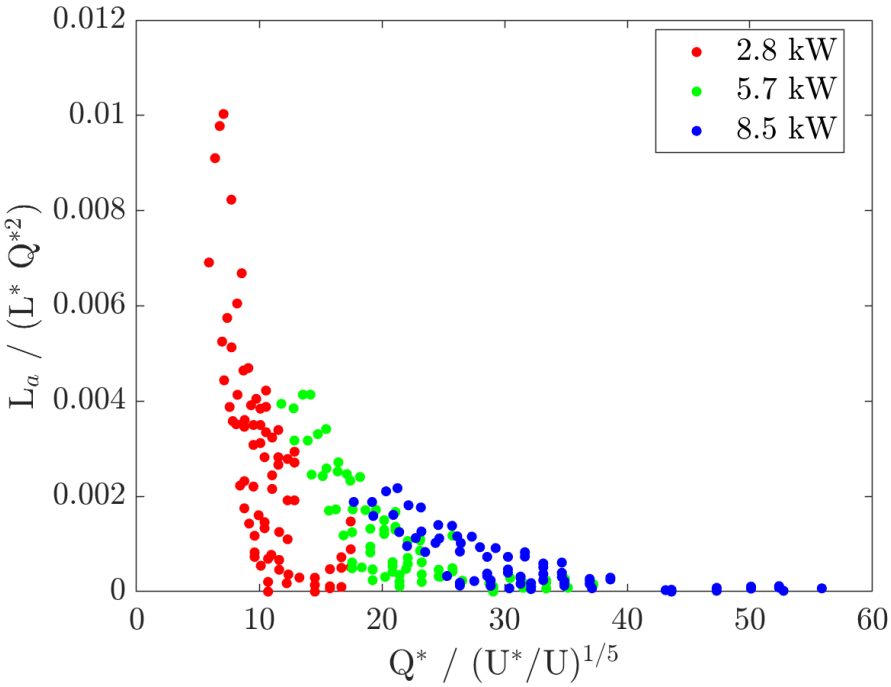

Figure 5.8: Predicting the non-dimensional attachment length using a combination of non-dimensional numbers.

5.3 Measurement Comparison

In order to compare the measurement techniques, the thresholds for flame attachment determined in previous sections and the results of the corresponding attachment length can be compared. Ideally, the flame attachment results would be identical between all measurement techniques. However, there is considerable discrepancy in attachment length between measurement techniques. Fig. 5.9 shows

several representative surface heat flux profiles along with attachment measurements from imaging and threshold thermocouple attachment. The attachment criteria across the measurement techniques appears to provide matching attachment lengths for some tests, but provide very different results for others. This could be because of differences in testing conditions that could not be controlled since all measurements were collected independently. The discrepancy in attachment lengths for some tests could also be due to the competing buoyant and forced flow forces creating different downstream plume behavior that is not visible in the imaging, or is only picked up by the thermocouples because of hot gases and no radiation from the sooty flame. An increased wind speed would force the plume of the flame further downstream, and increase the thermocouple readings, but not necessarily increase the visual flame attachment, or the radiant heat flux as much. This observational result indicates that relying on attachment measurements from imaging may not accurately reflect the downstream heating effects present with higher wind speeds.

Heat flux and temperature profiles were collected for a number of identical conditions to compare the two techniques. This, along with the attachment distance determined from imaging tests with the same external conditions, can be shown together in one figure, as in Fig. 5.10 where multiple test results are shown.

In Fig. 5.10 the imaging attachment threshold appears to occur at approximately the same distance that the thermocouple profile is at its peak, and before the heat flux profile dips below 15 kW/m^2. This is somewhat expected behavior. The differences between 5.10i and 5.10ii reinforces that a simple increase in wind speed at the same incline and HRR will push the heating profile further downstream

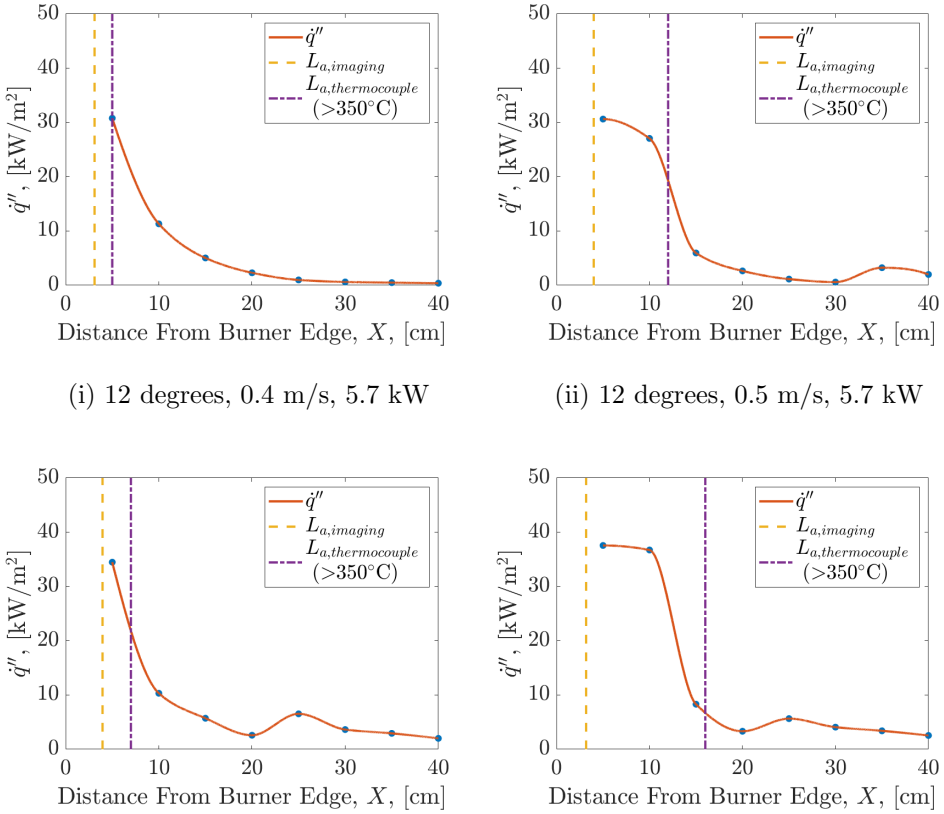

(i) 12 degrees, 0.4 m/s, 5.7 kW

(ii) 12 degrees, 0.5 m/s, 5.7 kW

(iii) 14 degrees, 0.3 m/s, 5.7 kW

(iv) 14 degrees, 0.4 m/s, 5.7 kW

Figure 5.9: Example profiles of average heat flux data from varying test conditions. The vertical lines represent the threshold taken for flame attachment from imaging and thermocouple data collection for a test with the same external conditions.

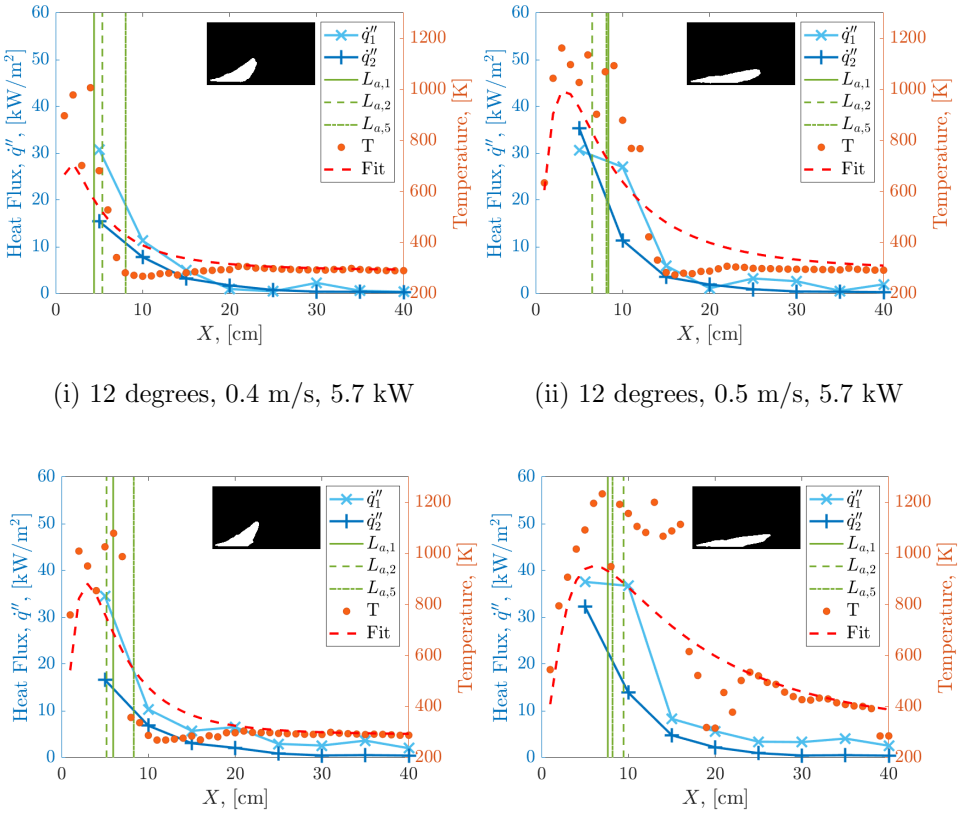

(i) 12 degrees, 0.4 m/s, 5.7 kW

(ii) 12 degrees, 0.5 m/s, 5.7 kW

(iii) 14 degrees, 0.3 m/s, 5.7 kW

(iv) 14 degrees, 0.4 m/s, 5.7 kW

Figure 5.10: Example data of each measurement technique from multiple test conditions. The vertical lines represent the flame attachment from imaging. Thermocouple measurement data and surface heat flux data provide profiles of the downstream heating in each instance. The binary image is the thresholded average of a 1 minute video.

of the burner. The profiles for the remainder of the tests that include thermocouple measurements are available in Appendix A.

The thermocouple attachment, defined as a reading above 350°C [44], can be directly compared to the imaging attachment length, as in Fig. 5.11. The linear trend shows that the thermocouple temperatures and flame imaging both showed a proportional increase in attachment length, although the thermocouple readings appear to detect the hot wind-blown plume further downstream, which is not visible in the imaging. The heat flux gauge data was not correlated in this instance, as it proved to be too spatially coarse to reveal a working trend.

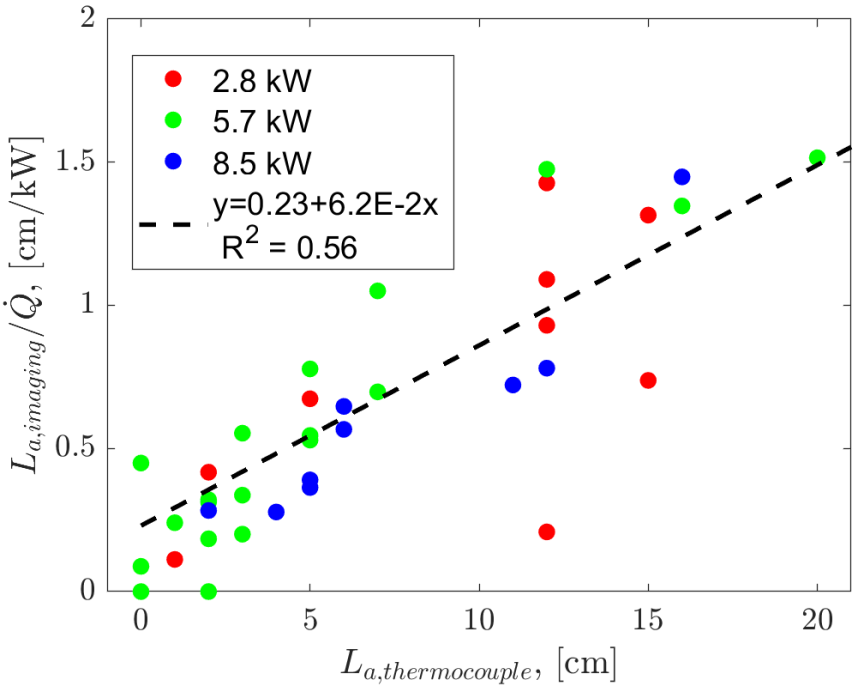

Figure 5.11: The thermocouple attachment results compared to the imaging attachment results. The thermocouple attachment is normalized by HRR, to collapse the data points, resulting in an R^2 value of 0.56.

Chapter 6: Conclusions

This controlled experimental study was able to isolate the effects of wind, slope and heat-release rate in a simplified, nearly 2-D geometry. As expected, increases in both wind and slope modified the geometry of flames to tilt towards the downstream surface and eventually attach, increasing both temperatures and heat fluxes downstream. The relationship between these quantities, however, is complex. The transition between a laminar unsteady lifted flame and completely laminar attached flame is nonlinear and is affected most strongly by the slope, followed by the heat-release rate of the burner or "fire size" and wind. While a generalized relationship or correlation to relate these three quantities was not found, an expansive dataset was formed and observations of the relationship between these quantities and the three measurement techniques used were made. The flame geometry under a wide variety of conditions has been explicitly outlined, and could potentially be extrapolated to different fire sizes and similar external conditions when coupled with numerical modeling in the future.

The relationship between the measurement techniques for measured flame attachment revealed that the visual attachment length typically depicts where the start of the downstream heating profile decay begins for both methods. Although,

the visual flame attachment is not able to detect the plume behavior after the visual flame, and therefore cannot predict the rate of decay of the heating profile. While previous studies with wind only identified the peak of the heating profile as the point where flames lifted from the surface, this work shows that the increased heat from the plume can continue well past where the visual flame is no longer in contact with the surface. The visual measurements of flame liftoff are useful for comparison with heat flux measurements, but do not accurately portray the heat applied downstream to the unburned fuel. The thermocouple measurements in front of the stationary flame capture what could be perceived as fine particle temperatures in a spreading fire and are useful in a numerical model when employing an ignition temperature assumption.

The limitations of this study largely pertain to the scale. Turbulence does not scale to realistic wildland fire spread scenarios, and the flame temperatures do not appropriately scale with flame sizes like the downstream heat flux will. Following previous studies, the results for wind are the most uniform and predictable, but the relationship with incline is clearly observable yet not fully understood. Despite this, the general relationship between momentum and buoyancy remain true at different scales. Studying the competing buoyant and momentum effects in a controlled manner that could then be separately translated to the large-scale is the primary reason such a small-scale study was employed. The data presented here will also be available to numerical modelers for future validation studies.

Appendix A: Downstream Heating Profiles

Figure A.1: Example data of each measurement technique from every test condition. The vertical lines represent the threshold taken for flame attachment from imaging, with thermocouple measurement data points and surface heat flux data points providing multiple profiles of the downstream heating in each instance. The image incorporated into the graph is the thresholded average image of a 1-minute video, that is tilted to the angle of incline applied during the experiment.

(i) 0 degrees, 0.3 m/s, 5.7kW

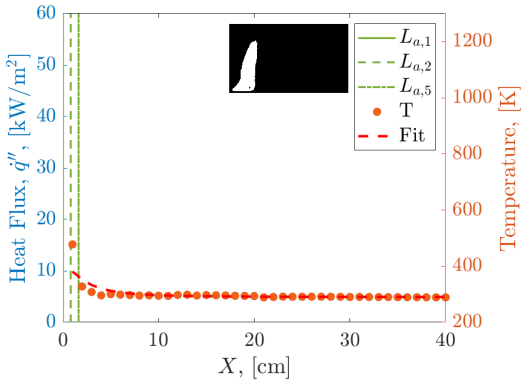

(ii) 0 degrees, 0.4 m/s, 5.7kW

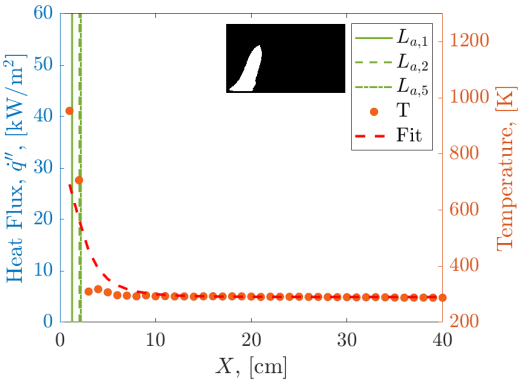

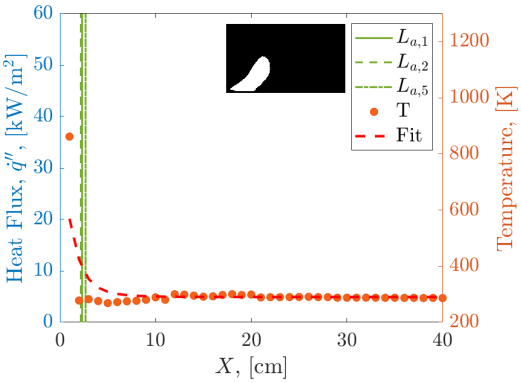

(iii) 0 degrees, 0.5 m/s, 5.7kW

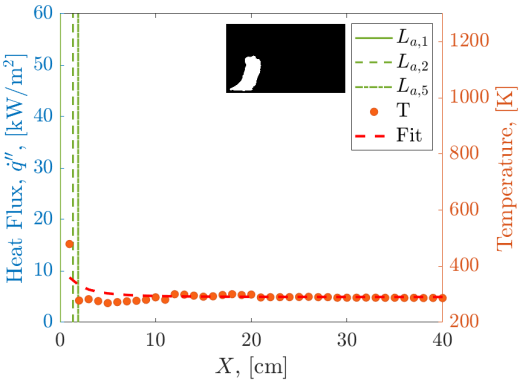

(iv) 6 degrees, 0.2 m/s, 5.7kW

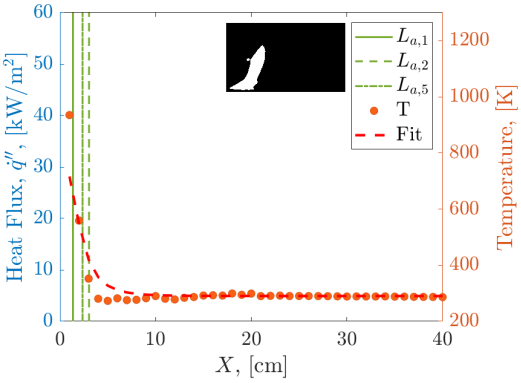

(v) 6 degrees, 0.3 m/s, 5.7kW

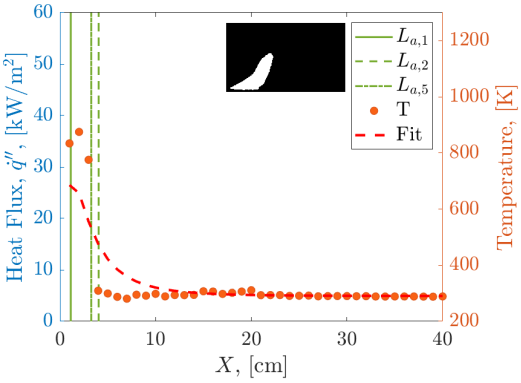

(vi) 6 degrees, 0.4 m/s, 5.7kW

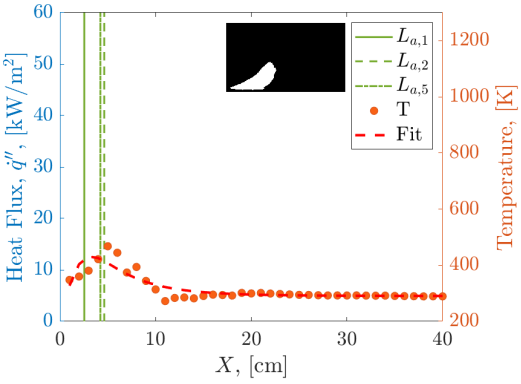

(vii) 6 degrees, 0.5 m/s, 5.7kW

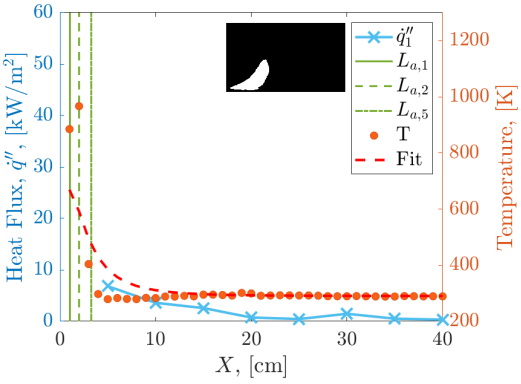

(viii) 10 degrees, 0.2 m/s, 5.7kW

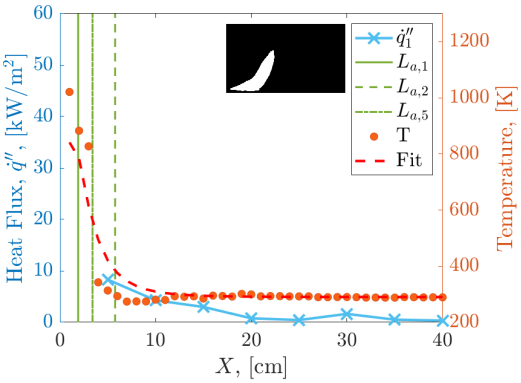

(i) 10 degrees, 0.3 m/s, 5.7kW

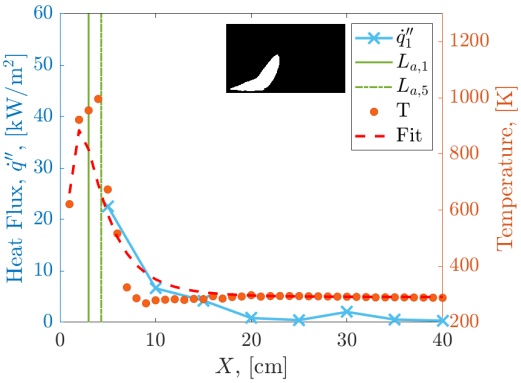

(ii) 10 degrees, 0.4 m/s, 5.7kW

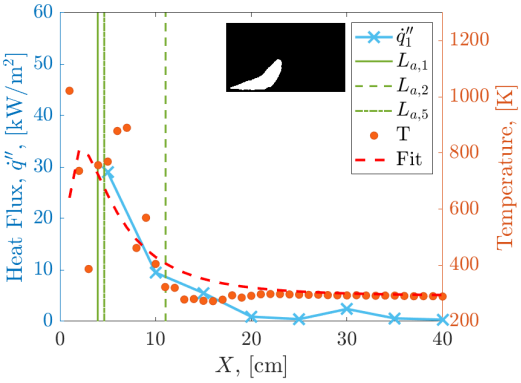

(iii) 10 degrees, 0.5 m/s, 5.7kW

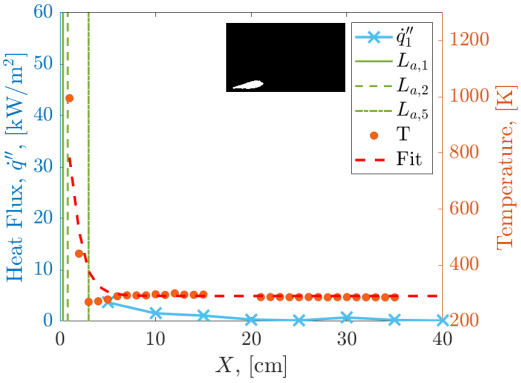

(iv) 12 degrees, 0.0 m/s, 2.8kW

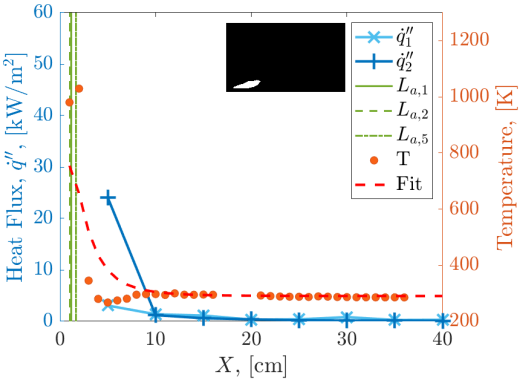

(v) 12 degrees, 0.2 m/s, 2.8kW

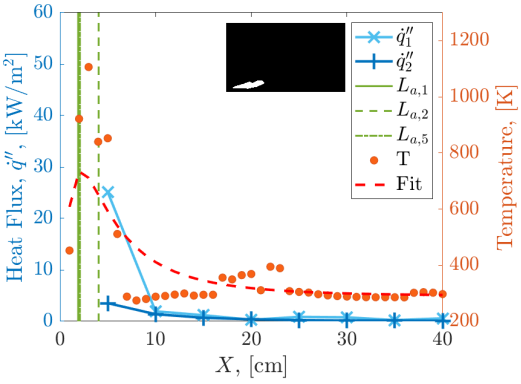

(vi) 12 degrees, 0.3 m/s, 2.8kW

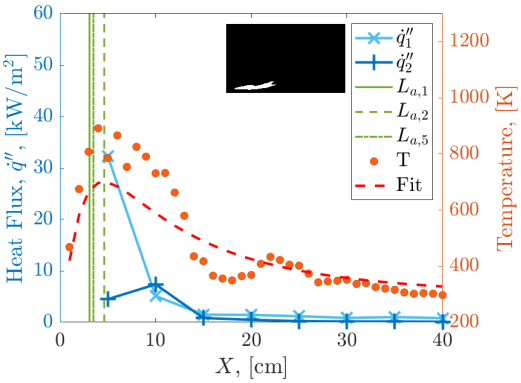

(i) 12 degrees, 0.4 m/s, 2.8kW

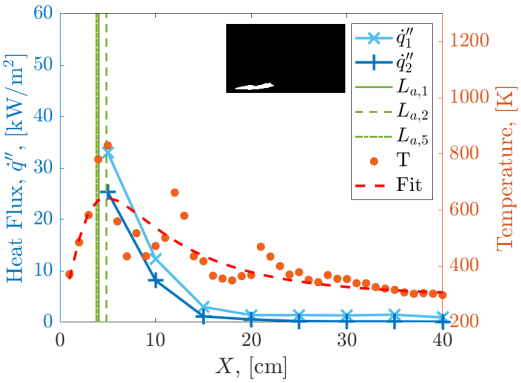

(ii) 12 degrees, 0.5 m/s, 2.8kW

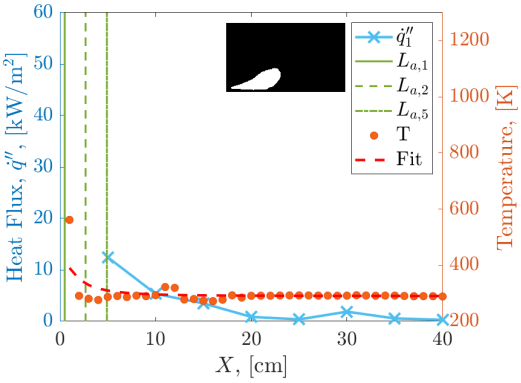

(iii) 12 degrees, 0.0 m/s, 5.7kW

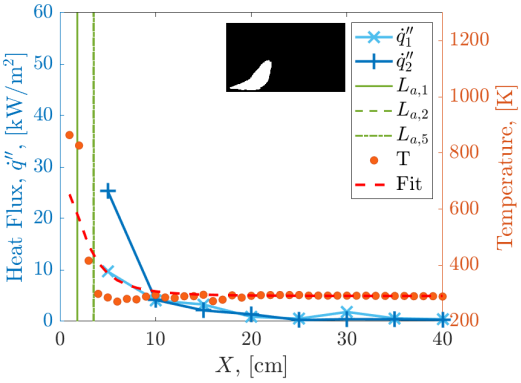

(iv) 12 degrees, 0.2 m/s, 5.7kW

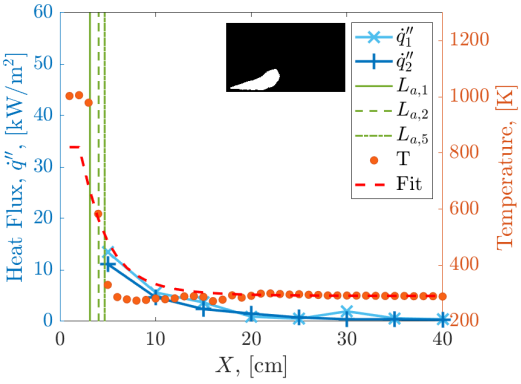

(v) 12 degrees, 0.3 m/s, 5.7kW

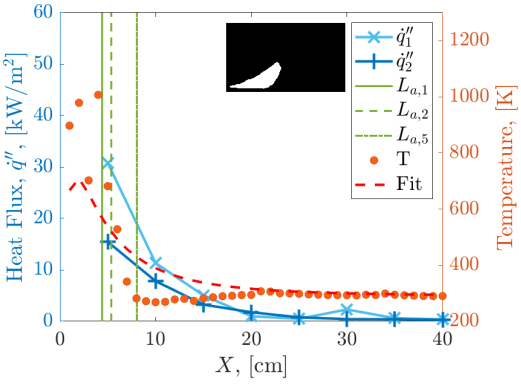

(vi) 12 degrees, 0.4 m/s, 5.7kW

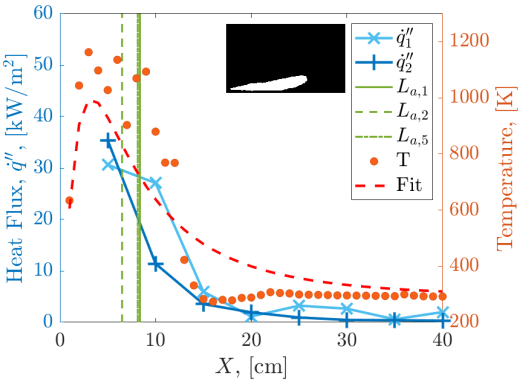

(i) 12 degrees, 0.5 m/s, 5.7kW

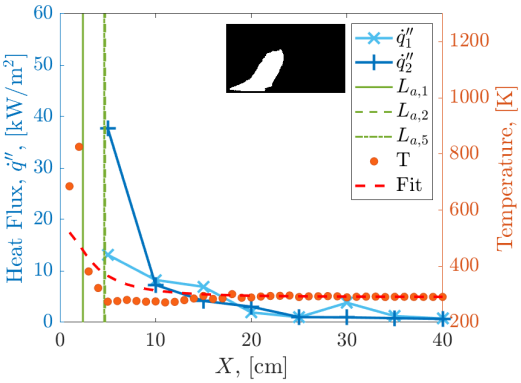

(ii) 12 degrees, 0.2 m/s, 8.5kW

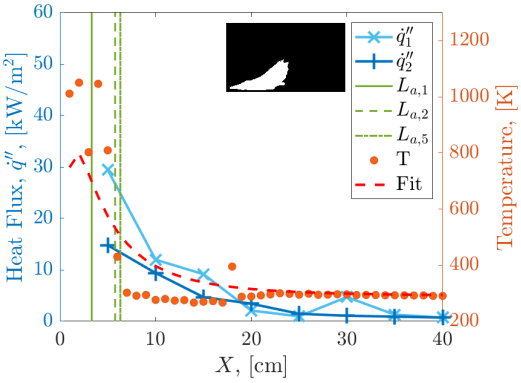

(iii) 12 degrees, 0.3 m/s, 8.5kW

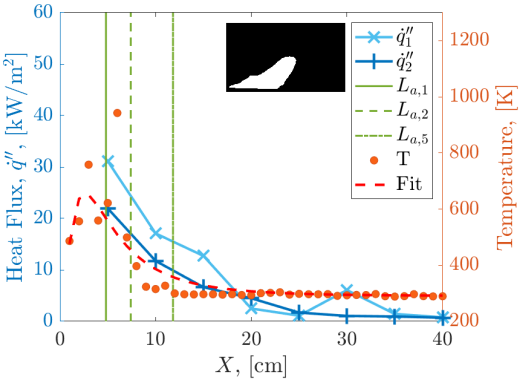

(iv) 12 degrees, 0.4 m/s, 8.5kW

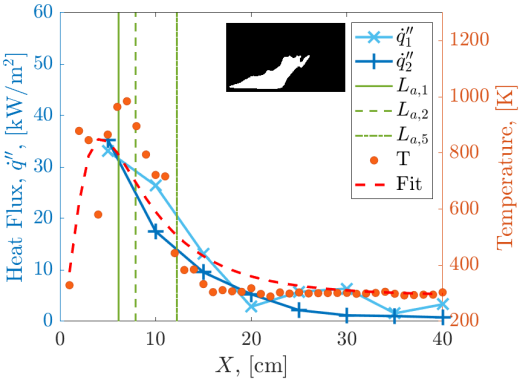

(v) 12 degrees, 0.5 m/s, 8.5kW

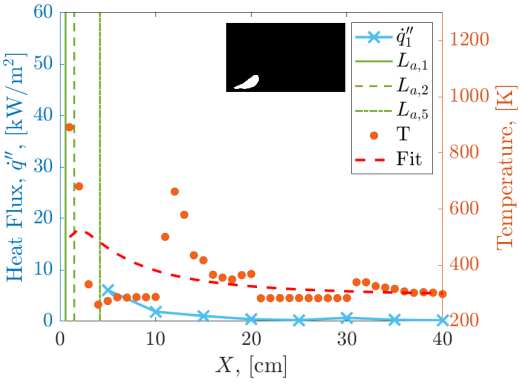

(vi) 14 degrees, 0.0 m/s, 2.8kW

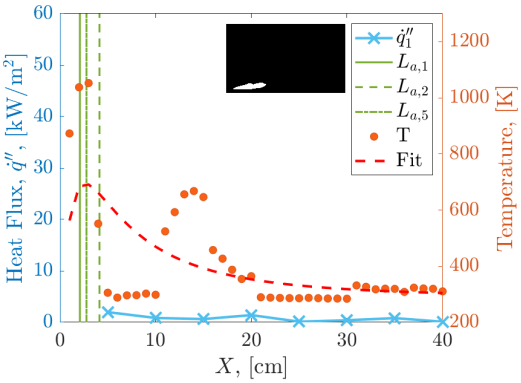

(i) 14 degrees, 0.2 m/s, 2.8kW

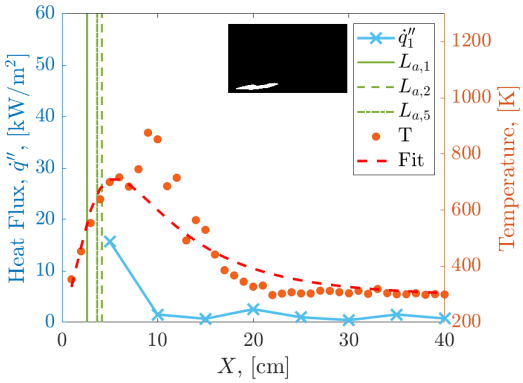

(ii) 14 degrees, 0.3 m/s, 2.8kW

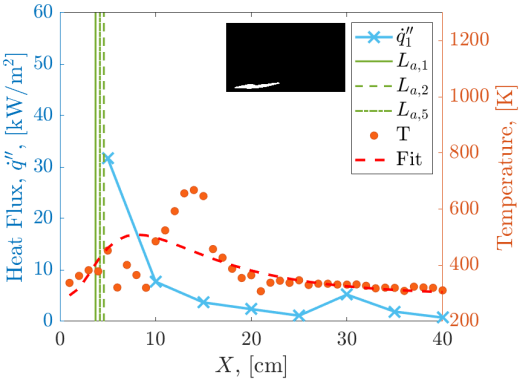

(iii) 14 degrees, 0.4 m/s, 2.8kW

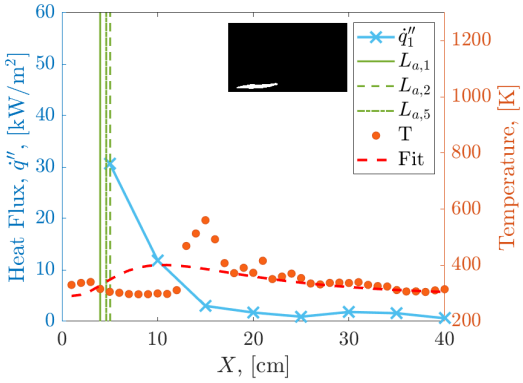

(iv) 14 degrees, 0.5 m/s, 2.8kW

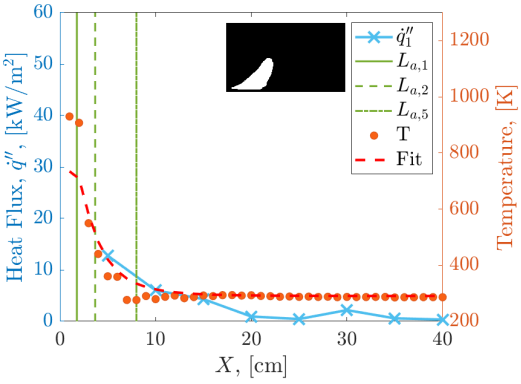

(v) 14 degrees, 0.0 m/s, 5.7kW

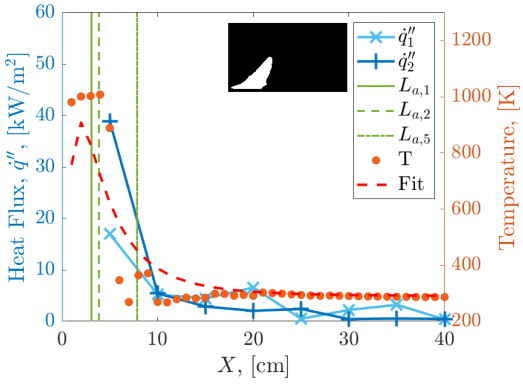

(vi) 14 degrees, 0.2 m/s, 5.7kW

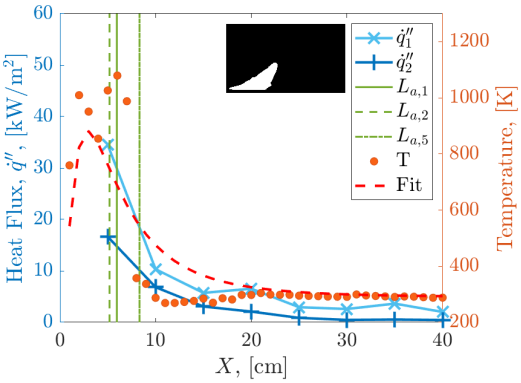

(i) 14 degrees, 0.3 m/s, 5.7kW

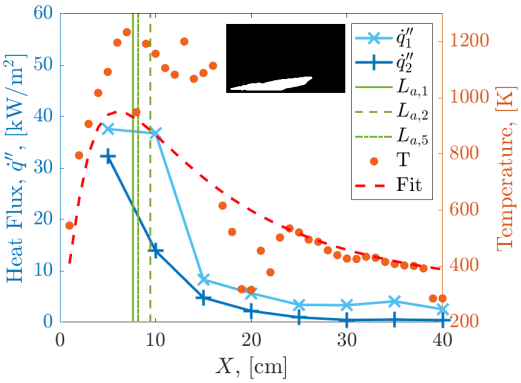

(ii) 14 degrees, 0.4 m/s, 5.7kW

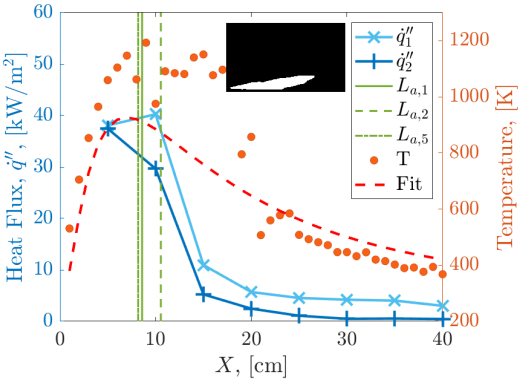

(iii) 14 degrees, 0.5 m/s, 5.7kW

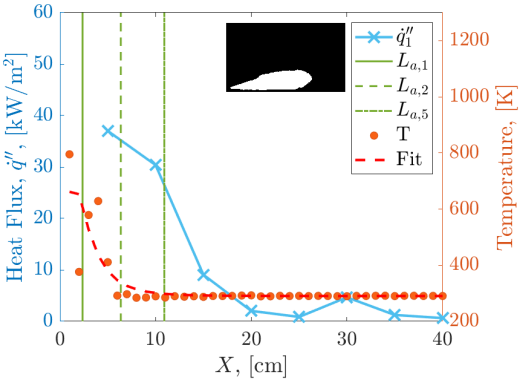

(iv) 14 degrees, 0.0 m/s, 8.5kW

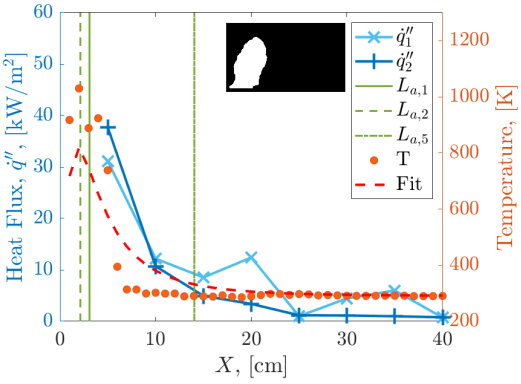

(v) 14 degrees, 0.2 m/s, 8.5kW

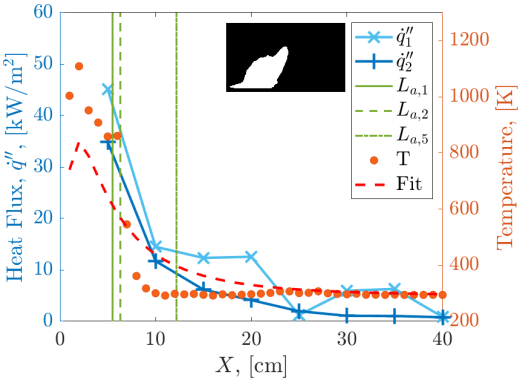

(vi) 14 degrees, 0.3 m/s, 8.5kW

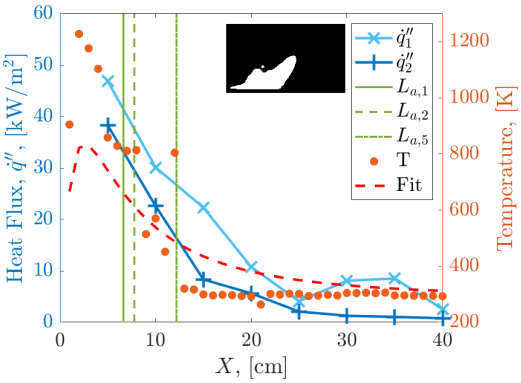

(i) 14 degrees, 0.4 m/s, 8.5kW

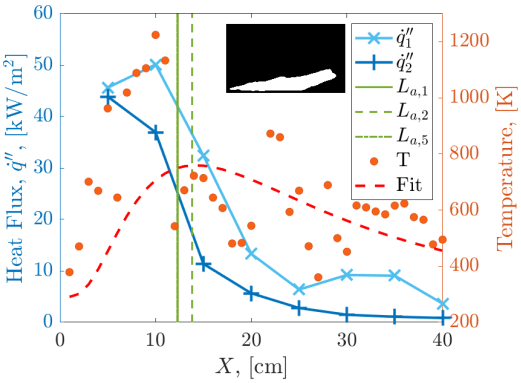

(ii) 14 degrees, 0.5 m/s, 8.5kW

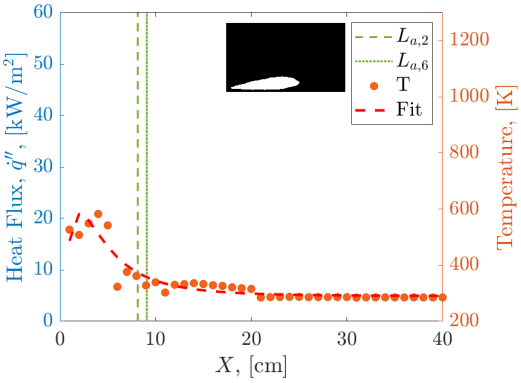

(iii) 18 degrees, 0.0 m/s, 5.7kW

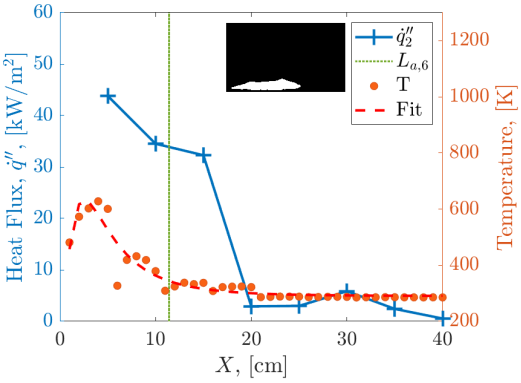

(iv) 18 degrees, 0.2 m/s, 5.7kW

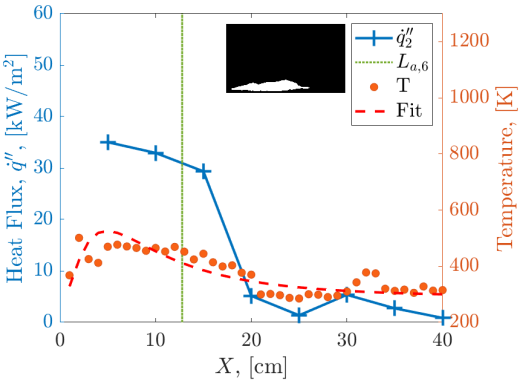

(v) 18 degrees, 0.3 m/s, 5.7kW

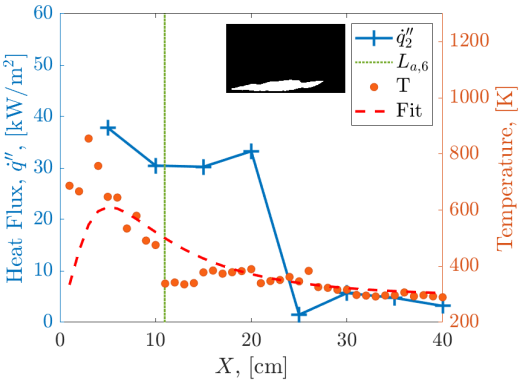

(vi) 18 degrees, 0.4 m/s, 5.7kW

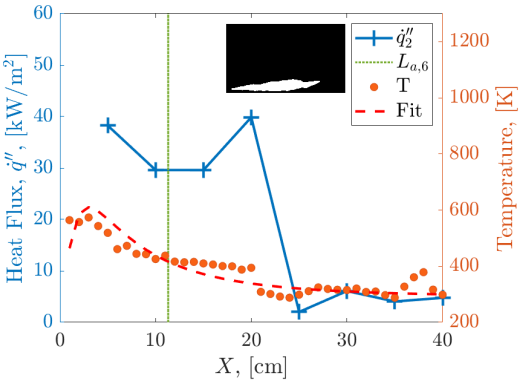

(i) 18 degrees, 0.5 m/s, 5.7kW

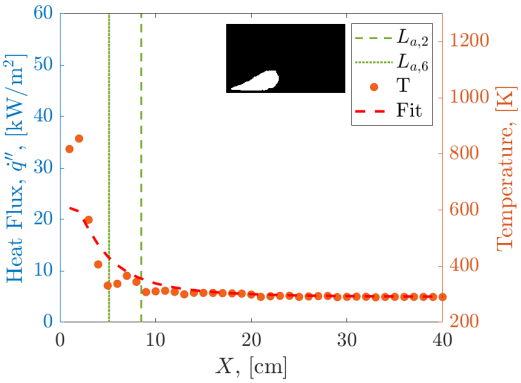

(ii) 16 degrees, 0.0 m/s, 5.7kW

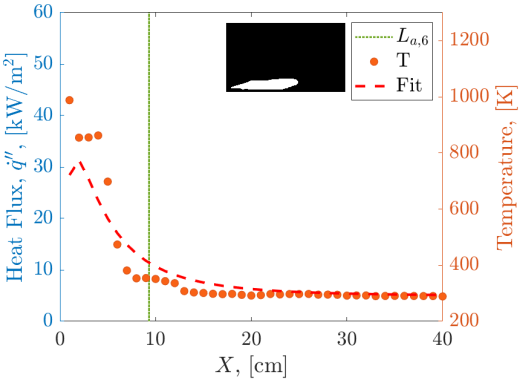

(iii) 16 degrees, 0.2 m/s, 5.7kW

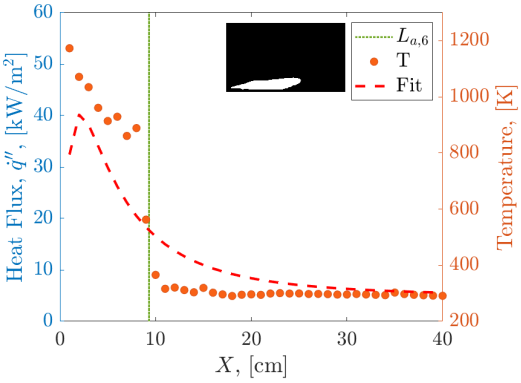

(iv) 16 degrees, 0.3 m/s, 5.7kW

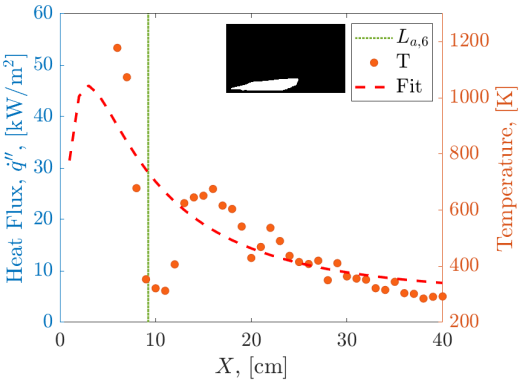

(v) 16 degrees, 0.4 m/s, 5.7kW

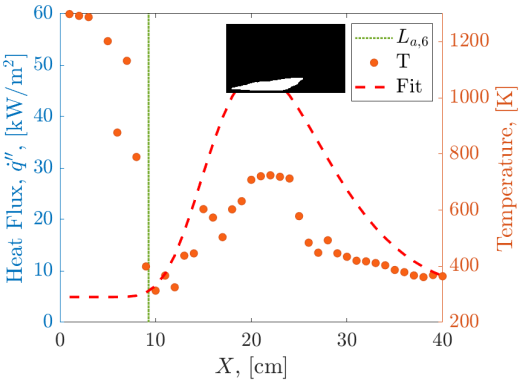

(vi) 16 degrees, 0.5 m/s, 5.7kW

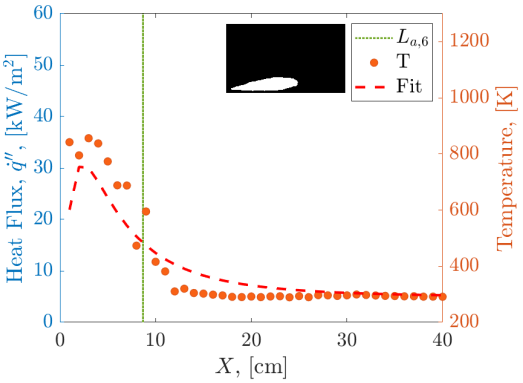

(i) 20 degrees, 0.0 m/s, 5.7kW

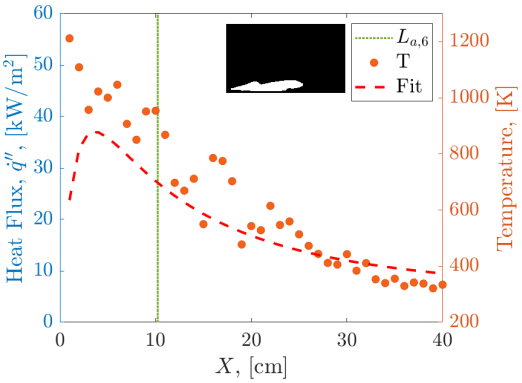

(ii) 20 degrees, 0.2 m/s, 5.7kW

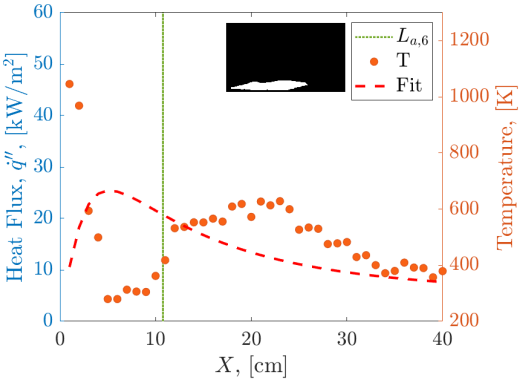

(iii) 20 degrees, 0.3 m/s, 5.7kW

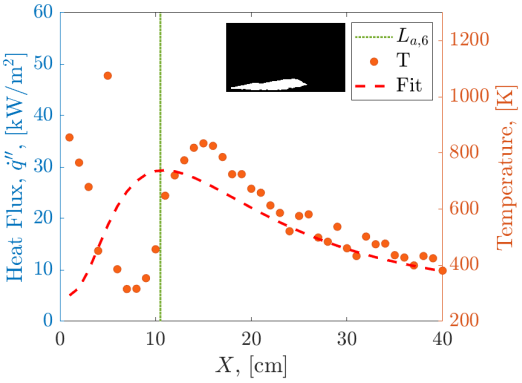

(iv) 20 degrees, 0.4 m/s, 5.7kW

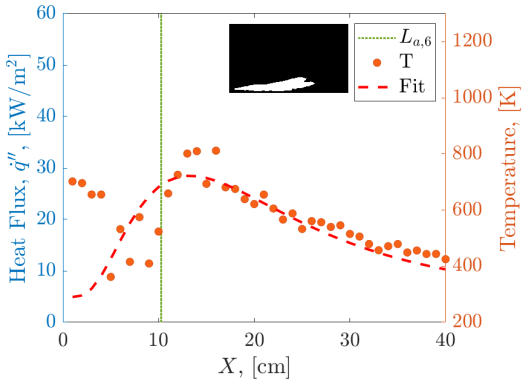

(v) 20 degrees, 0.5 m/s, 5.7kW

Bibliography

[1] National Interagency Fire Center. Suppression costs (1995-2018). URL: https://www.nifc.gov/fireInfo/fireInfo_documents/SuppCosts.pdf, 2018.

[2] United States Forest Service. Rising cost of wildfire operations: Effects on forest service's non-fire work. URL: https://www.fs.fed.us/sites/default/files/2015-Fire-Budget-Report.pdf, 2015.

[3] R. C. Rothermel. A mathematical model for predicting fire spread in wildland fuels. In *Res. Pap. INT-115.*, U.S. Department of Agriculture, Intermountain Forest and Range Experiment Station, page 40 p, Ogden, UT, 1972.

[4] I. Noble, A. Gill, and G. Bary. Mcarthur's fire-danger meters expressed as equations. *Australian Journal of Ecology*, 5:201 – 203, 07 2006.

[5] Y. Wu, H.J. Xing, and G. Atkinson. Interaction of fire plume with inclined surface. *Fire Safety Journal*, 35(4):391 – 403, 2000.

[6] F.A. Williams. Mechanisms of fire spread. *Symposium (International) on Combustion*, 16(1):1281–1294, 1977.

[7] J. G. Quintiere. *Fundamentals of fire phenomena*. Wiley, 2008.

[8] P.H. Thomas. Some aspects of the growth and spread of fire in the open. *Forestry*, 40(2):139–164, 1967.

[9] G.M. Byram and K.P. Davis. *Forest fire: control and use*. McGraw-Hill Book Company, 1959.

[10] J.D. Cohen and M.A. Finney. An examination of fuel particle heating during fire spread. *Viegas, D. X., ed. Proceedings of the VI International Conference on Forest Fire Research*, page 15–18, Nov 2010.

[11] H. E. Anderson. Heat transfer and fire spread. 1969.

[12] M.A. Finney, J.D. Cohen, J. D. Forthofer, S.S. Mcallister, M.J. Gollner, D.J. Gorham, K. Saito, N.K. Akafuah, B.A. Adam, J.D. English, and et al. Role of buoyant flame dynamics in wildfire spread. *Proceedings of the National Academy of Sciences*, 112(32):9833–9838, 2015.

[13] M.J. Gollner, X. Huang, J. Cobian, A.S. Rangwala, and F.A. Williams. Experimental study of upward flame spread of an inclined fuel surface. *Proceedings of the Combustion Institute*, 34(2):2531 – 2538, 2013.

[14] V.B. Apte, R.W. Bilger, A.R. Green, and J.G. Quintiere. Wind-aided turbulent flame spread and burning over large-scale horizontal pmma surfaces. *Combustion and Flame*, 85(1-2):169–184, 1991.

[15] J. Dold and A. Zinoviev. Fire eruption through intensity and spread rate interaction mediated by flow attachment. *Combustion Theory and Modelling - COMBUST THEORY MODEL*, 13:763–793, 12 2009.

[16] W. Tang, C.H. Miller, and M.J. Gollner. Local flame attachment and heat fluxes in wind-driven line fires. *Proceedings of the Combustion Institute*, 36(2):3253–3261, 2017.

[17] M.J. Gollner and E.T. Sluder. *Understanding the Influence of Wind and Slope On Flames in Wildland Fires*. M.s. thesis, University of Maryland, 2018.

[18] W. Tang, D.J. Gorham, M.A. Finney, S.S. Mcallister, J.D. Cohen, J.D. Forthofer, and M.J. Gollner. An experimental study on the intermittent extension of flames in wind-driven fires. *Fire Safety Journal*, 91:742–748, 2017.

[19] D.X. Viegas. Parametric study of an eruptive fire behaviour model. *International Journal of Wildland Fire*, 15(2):169, 2006.

[20] F. Morandini, X. Silvani, D. Honoré, G. Boutin, A. Susset, and R. Vernet. Slope effects on the fluid dynamics of a fire spreading across a fuel bed: Piv measurements and oh* chemiluminescence imaging. *Experiments in Fluids*, 55(8), 2014.

[21] K. Moodie and S.f. Jagger. The kings cross fire: Results and analysis from the scale model tests. *Fire Safety Journal*, 18(1):83–103, 1992.

[22] D.D. Drysdale and A.J.R. Macmillan. Flame spread on inclined surfaces. *Fire Safety Journal*, 18(3):245–254, 1992.

[23] D.D. Drysdale, A.J.R. Macmillan, and D. Shilitto. The kings cross fire: Experimental verification of the 'trench effect'. *Fire Safety Journal*, 18(1):75–82, 1992.

[24] D.A. Smith. Measurements of flame length and flame angle in an inclined trench. *Fire Safety Journal*, 18(3):231 – 244, 1992.

[25] Y. Pizzo, J.L. Consalvi, and B. Porterie. A transient pyrolysis model based on the b-number for gravity-assisted flame spread over thick pmma slabs. *Combustion and Flame*, 156(9):1856–1859, 2009.

[26] W. Xie and P.E. DesJardin. An embedded upward flame spread model using 2d direct numerical simulations. *Combustion and Flame*, 156(2):522 – 530, 2009.

[27] M.J. Gollner, C.H. Miller, W. Tang, and A.V. Singh. The effect of flow and geometry on concurrent flame spread. *Fire Safety Journal*, 91:68 – 78, 2017. Fire Safety Science: Proceedings of the 12th International Symposium.

[28] H.T. Loh and A.C. Fernandez-Pello. A study of the controlling mechanisms of flow assisted flame spread. *Symposium (International) on Combustion*, 20(1):1575 – 1582, 1985. Twentieth Symposium (International) on Combustion.

[29] C.P. Mao, A.C. Fernandez-Pello, and P.J. Pagni. Mixed convective burning of a fuel surface with arbitrary inclination. *Journal of Heat Transfer*, 106(2):304–309, Jan 1984.

[30] G.T. Atkinson, D.D. Drysdale, and Y. Wu. Fire driven flow in an inclined trench. *Fire Safety Journal*, 25(2):141 – 158, 1995.

[31] J. de Ris and L. Orloff. The role of buoyancy direction and radiation in turbulent diffusion flames on surfaces. *Symposium (International) on Combustion*, 15(1):175 – 182, 1975. Fifteenth Symposium (International) on Combustion.

[32] A.C. Fernandez-Pello. Flame spread in a forward forced flow. *Combustion and Flame*, 36:63 – 78, 1979.

[33] J.L. Consalvi, Y. Pizzo, and B. Porterie. Numerical analysis of the heating process in upward flame spread over thick pmma slabs. *Fire Safety Journal*, 43(5):351 – 362, 2008.

[34] K. Tsai, J. Turnbull, G. Will, and D. Drysdale. Upward flame spread: Heat transfer to the unburned surface. *Fire Safety Science*, 7:117–127, 01 2003.

[35] G.H. Markstein and J. de Ris. Upward fire spread over textiles. *Symposium (International) on Combustion*, 14(1):1085–1097, 1973.

[36] O. Korobeinichev, M. Gonchikzhapov, A. Tereshchenko, I. Gerasimov, A. Shmakov, A. Paletsky, and A. Karpov. An experimental study of horizontal flame spread over pmma surface in still air. *Combustion and Flame*, 188:388 – 398, 2018.

[37] B.K. Dhurandher, R. Kumar, A.K. Dhiman, A. Gupta, and P.K. Sharma. An experimental study of vertical centreline temperature and velocity profile of buoyant plume in cubical compartment. *Journal of the Brazilian Society of Mechanical Sciences and Engineering*, 39(5):1813–1822, 2016.

[38] W.C. Strahle and M. Muthukrishnan. Thermocouple time constant measurement by cross power spectra. *AIAA Journal*, 14(11):1642–1644, 1976.

[39] X. Ren, D. Zeng, Y. Wang, G. Xiong, G. Agarwal, and M.J. Gollner. Temperature measurement of a turbulent buoyant ethylene diffusion flame using a dual-thermocouple technique. EasyChair Preprint no. 2399, EasyChair, 2020.

[40] E.J. Weckman and A.B. Strong. Experimental investigation of the turbulence structure of medium-scale methanol pool fires. *Combustion and Flame*, 105(3):245 – 266, 1996.

[41] A. Ballantyne and J.B. MOSS. Fine wire thermocouple measurements of fluctuating temperature. *Combustion Science and Technology*, 17(1-2):63–72, 1977.

[42] M. Tagawa and Y. Ohta. Two-thermocouple probe for fluctuating temperature measurement in combustion—rational estimation of mean and fluctuating time constants. *Combustion and Flame*, 109(4):549–560, 1997.

[43] P. Santoni, T. Marcelli, and E. Leoni. Measurement of fluctuating temperatures in a continuous flame spreading across a fuel bed using a double thermocouple probe. *Combustion and Flame*, 131(1):47 – 58, 2002.

[44] M.A. Finney, J.D. Forthofer, and I.C. Grenfell. A study of flame spread in engineered cardboard fuel beds part i: Correlations and observations of flame spread. *Seventh International Symposium on Scale Modeling*, 2013.

[45] J.S. Lozano. *An investigation of surface and crown fire dynamics in shrub fuels.* PhD thesis, University of California: Riverside. 245 p, 2011.

[46] W. Tachajapong, J.S. Lozano, S. Mahalingam, and X. Zhou. Experimental and numerical modeling of shrub crown fire initiation, 2009.

[47] L. Cattafesta, C. Bahr, and J. Mathew. *Fundamentals of Wind-Tunnel Design.* 12 2010.

[48] F Albini. A model for the wind-blown flame from a line fire. *Combustion and Flame*, 43:155–174, 1981.

[49] P.J. Woodburn and D.D. Drysdale. Fires in inclined trenches: the dependence of the critical angle on the trench and burner geometry. *Fire Safety Journal*, 31(2):143–164, 1998.

[50] Z. Yang and H. Chen. Experimental study on flame geometry along the inclined surface with and without sidewalls by using a gas burner. *Procedia Engineerin*, 211:925 – 933, 2018. 2017 8th International Conference on Fire Science and Fire Protection Engineering (ICFSFPE 2017).

[51] G.H. Markstein and J. de Ris. Upward fire spread over textiles. *Symposium (International) on Combustion*, 14(1):1085 – 1097, 1973. Fourteenth Symposium (International) on Combustion.